**Diploma Thesis**

# Non-Linear Finite Element Simulations of Nanoindentation in Gallium Nitride Considering Fracture Mechanics and Plasticity

carried out for the purpose of obtaining the degree of
Master of Science (MSc or Dipl.-Ing.), submitted at TU Wien,
Faculty of Mechanical and Industrial Engineering, by

**Valentin Johannes UNGER**

Mat. Nr.: 01027151
Thurnhartinger Straße 2
4062 Kirchberg-Thening

under the supervision of
Associate Prof. Dipl.-Ing. Dr. techn. Heinz Pettermann
Institute of Lightweight Design and Structural Biomechanics

reviewed by

Heinz Pettermann
ILSB, E317

Jürgen Stampfl
WWWT, E308

Diploma Thesis

This thesis has been developed as a part of a cooperation project with the Kompetenzzentrum für Automobil- und Industrieelektronik GmbH, Villach (KAI).

I confirm, that going to press of this thesis needs the confirmation of the examination committee.

*Affidavit*

I declare in lieu of oath, that I wrote this thesis and performed the associated research myself, using only literature cited in this volume. If text passages from sources are used literally, they are marked as such. I confirm that this work is original and has not been submitted elsewhere for any examination, nor is it currently under consideration for a thesis elsewhere.

Vienna, October 2018

_____

Signature

# Acknowledgment

This thesis is part of a project that has received funding from the Electronic Component Systems for European Leadership Joint Undertaking under grant agreement No 662133. In the Power-Base project this Joint Undertaking receives support from the European Union's Horizon 2020 research and innovation program and from Austria, Belgium, Germany, Italy, Netherlands, Norway, Slovakia, Spain and the United Kingdom.

My deepest gratitude goes to my thesis adviser Associate Prof. Dipl.-Ing. Dr.techn. Heinz Pettermann for his support, the ideas, and the valuable suggestions throughout the progression of this thesis. His helpful feedback and challenges over the last few month taught me a lot. I would like to thank the ILSB staff for the sincere office atmosphere and especially Dipl.-Ing. Paul Hoffmann and Dr. Martin Springer for various inspiring discussions.

I am also very thankful for the mentoring during my employment at the Kompetenzzentrum für Automobil- und Industrieelektronik GmbH, Villach. Special thanks go to my industrial supervisor Dr. Balamurugan Karunamurthy who introduced me to this interesting field of study. Moreover, I would like to thank Dipl.-Ing. Josef Fugger and Dr. Michael Nelhiebel for their valuable support and Dr. Johannes Zechner for the conducted experiments.

None of this would have been possible without the support and patience of my family during my studies. I am also particularly grateful to my friends and colleagues for their help and the necessary distractions throughout the years.

Finally, I would like to thank Magdalena for being the wonderful person she is.

# Abstract

Modern power semiconductor materials need to withstand high power densities, while devices are getting downsized to meet the industrial demands.

In order to study the mechanical behaviour and the limitations of these brittle layered electronics materials, often nanoindentation experiments are conducted. For the purpose of supporting the instrumented indentation testing, the Finite Element Method in combination with a cohesive zone model and anisotropic Hill's plasticity is applied. Special focus is laid on Gallium Nitride (GaN) on Silicon (Si) stacks penetrated by a Berkovich indenter tip. The main goal of this thesis is to establish a non-linear nanoindentation Finite Element model to predict crack emergence and propagation in the layers including various residual stress states, that possibly arise during the wafer fabrication. The developed numerical model is able to predict both, the energy dissipation due to plastic deformation as well as material fracture.

The numerically predicted load-penetration curves show a good compliance with the experimental data, obtained by the KAI GmbH, Villach. The simulation results predict quarter-penny cracks in GaN and Si, depending on the indentation depth and residual stress state. Various influences on the mechanical behaviour, and especially the fracture behaviour are studied. Residual stresses are found to show a strong effect on the fracture behaviour of GaN. Tensile stresses lead to a temporarily unstable crack growth, whereas compressive stresses tend to mitigate the crack propagation. The non-linear simulations give the possibility to investigate different stack designs in rather short time and yield information about the stress state and sub-surface cracks during the indentation process.

# Kurzfassung

Moderne Leistungshalbleitermaterialien müssen in der Lage sein große Leistungsdichten zu ertragen, obwohl die Bauelemente kontinuierlich verkleinert werden, um den Ansprüchen der Industrie gerecht zu werden.

Um das mechanische Verhalten sowie die Anwendungsgrenzen dieser spröden, geschichteten Materialien während einer instrumentierten Eindringprüfung zu untersuchen, wird die Finite Elemente Methode in Verbindung mit einem Kohäsivzonenmodell und der anisotropen Hill Plastizität angewendet. Besonderes Augenmerk liegt dabei auf Galliumnitrid (GaN) auf Silizium (Si) Schichten, die mit einem Berkovich Indenter geprüft werden. Das Ziel dieser Arbeit ist es ein nicht lineares Nanoindentierungs Finite Elemente Modell zu entwickeln, das Rissentwicklung und Rissausbreitung in diesen Schichten vorhersagt. Oft herrschen in den Lagen erhebliche Eigenspannungen, die während der Herstellung entstehen können. Das erstellte numerische Modell ist in der Lage die Dissipation aufgrund von plastischer Verformung, als auch aufgrund von Bruch abzubilden.

Die berechneten Last-Eindring-Kurven zeigen eine gute Übereinstimmung mit den experimentellen Daten der KAI GmbH, Villach. Die Simulationsergebnisse zeigen auftretende Quarter-Penny Risse in GaN und Si, die stark von der Eindringtiefe und den Restspannungen abhängen. Verschiedene Einflüsse auf das mechanische und vor allem auf das Bruchverhalten werden untersucht. Die Eigenspannungen haben eine große Auswirkung auf das Bruchverhalten in GaN. Zugspannungen führen zu einer teilweise instabilen Rissausbreitung. Druckspannungen vermindern die Ausbreitung des Risses. Das nicht lineare Modell gibt die Möglichkeit zur Untersuchung von vielen Schichtaufbauten in kurzer Zeit und ermöglicht die Untersuchung der Spannungen und Risse unter der Oberfläche.

# Table of Contents

# Chapter 1

# Introduction

## 1.1 Motivation

Power semiconductors have evolved steadily over recent years, leading to new high-performance devices. The Gallium Nitride (GaN) on Silicon (Si) technology, using the direct epitaxial growth of GaN on the substrate is a worthwhile production option in the high-performance power semiconductor industry [21]. Devices, based on single crystal GaN are characterised by their exceptional efficiency and high voltage operation, their high power density and their high frequency bandwidths. Intensive research focus has been on not only the electrical properties of GaN but also production-worthiness and long-term usage of GaN-on-Si devices [21, 23].

Due to the epitaxial growth processes, the non-conformance of thermo-mechanical properties as well as the lattice mismatch between GaN layers and the substrate, residual stresses arise during wafer fabrication processes. To bypass this large non-compliance between GaN and Si, it is crucial to have a suitable number of transition layers on the substrate. Common sub-layer materials are Aluminium Gallium Nitride (AlGaN) and Aluminium Nitride (AlN), which build up a heterostructure to mitigate the residual stresses in the wafer. However, this prevention can only reduce the stresses to a certain degree [21, 22].

Due to the residual stresses and the brittle nature of GaN, it is of interest to gain more information about the mechanical behaviour of GaN. Therefore, nanoindentation experiments are conducted in order to study the risk of fracture. This material testing is often very complex and time consuming, depending on many uncertain and precarious factors [9].
For the purpose of supporting these experiments, numerical simulations using the Finite Element Method (FEM) are advantageous. Complex non-linear simulations enable the investigation of different stack designs in rather short time and yield information about the stress state and sub-surface cracks during the nanoindentation process.

### 1.1.1 Background Work

This work is the third one in a series of diploma theses focused on Finite Element simulations of nanoindentation experiments in single crystal materials used in power semiconductors. Both preceding theses have been carried out in collaboration with KAI GmbH, Villach as well.
In the first thesis, starting in 2015, Clemens Reichel [28] has examined the crack formation and propagation in layered electronics structures assuming solely elastic material behaviour before fracturing. In Figure 1.1(a) a load-penetration curve of a simulation from [28] is depicted. A deviation between the loading- and unloading curves indicates the dissipation of energy during the indentation process. Even for high indentation depths exceeding 1.5 µm the results in the load-penetration diagrams have shown only minimal energy dissipation, despite the formation of large median cracks. This has led to the hypothesis of another major energy dissipation mechanism in nanoindentation of brittle materials. Furthermore, it has been indicated in [28] that residual stresses in the multilayered structure have a high influence on the

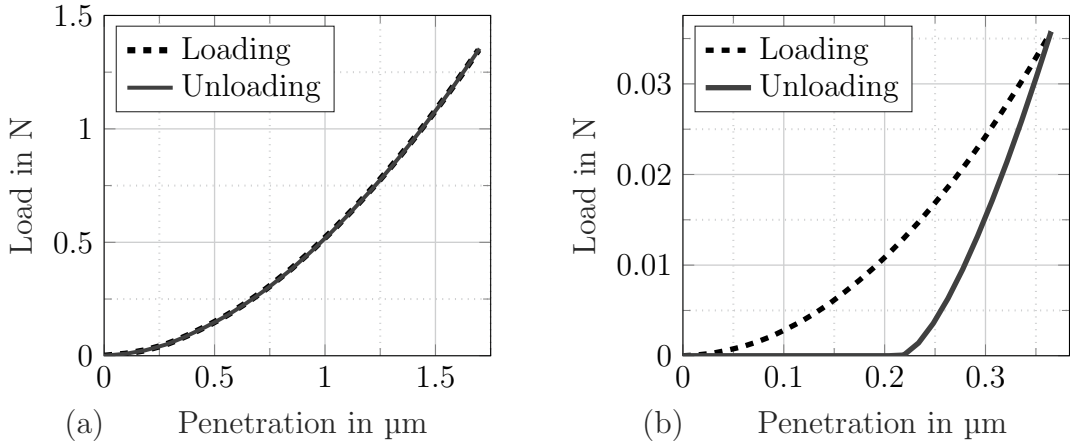


**Figure 1.1:** Predicted load-penetration curves. (a) Indentation depth 1.7 µm, no visible energy dissipation [28]. (b) Indentation depth 0.365 µm, energy dissipated during the indentation process [11].

fracture behaviour of GaN.

The second thesis has been conducted by Paul Hoffmann [11] investigating the plastic behaviour of Gallium Nitride. P. Hoffmann has shown that the inclusion of plasticity led to a much better compliance with the experimental nanoindentation results. Figure 1.1(b) shows a predicted load-penetration curve for an indentation depth of 0.365 µm. The loading- and unloading curve differ strongly, pointing out that the plasticity cannot be neglected in nanoindentation simulations. However, the modelling of cracks has exceeded the scope of that thesis. It has been shown in [11] that the incorporation of residual stresses in the model has no significant effect on the plastic behaviour and the load-penetration curve in nanoindentation simulations.

### 1.1.2 Aims and Objectives

The aim of the present thesis is to establish a Finite Element model of nanoindentation experiments and run non-linear simulations to study the fracture behaviour in combination with the anisotropic plasticity. On the basis of the two preceding theses, the modelling approaches are developed further. The numerical model should be able

to predict both, the dissipation of energy due to plastic deformation as well as the crack formation and propagation.
The emergence of cracks during the indentation and furthermore the final crack size and shape needs to be studied and the influences of various factors investigated.
In order to validate the simulations, experiments have been carried out at the KAI, Villach and can be compared to the numerical results.
Furthermore, the investigation of the effect of various residual stress states in the stacked layers is of great interest.

## 1.2 Nanoindentation Experiments

Nanoindentation experiments are very commonly applied means of instrumented indentation testing (IIT) of materials. It is a technique for obtaining information about the elastic, plastic as well as the fracture behaviour of materials.

### 1.2.1 Experimental Procedure

This section gives an overview of this material testing procedure as reported in the literature by J. Hay [9].

At the start of the experiment the indenter tip approaches the tested material until they are in contact. After that the tip is pressed into the material until the maximum force or penetration depth is reached. The measurements can either be force or displacement controlled. In contrast to traditional hardness tests the force and penetration are measured continuously. After the point of maximum load is reached, the force is held constant for a specific dwell time to observe potential time dependent phenomena. During the unloading of the sample the indenter tip is again held constant for another dwell time where the force reaches about 10 % of the peak load. Finally the indenter is withdrawn from the material. Figure 1.2(a) shows a schematic

representation of a nanoindentation experiment of a multilayered structure on a substrate using a Berkovich tip. In the sketch the sample is depicted after the unloading, showing a residual imprint as well as cracks emerging from the indenter edges. Using the measured force and indentation depth during the experiment a load-penetration curve can be obtained. The reaction force is plotted against the penetration depth, resulting in a loading- and an unloading curve. In Figure 1.2(b) a sketch of a load-penetration curve is depicted. The area in between the two curves corresponds to the dissipated energy during the nanoindentation experiment. The point where the unloading curve meets the abscissa, displays the residual indentation depth. During the measurements so-called pop-in events can occur. They are a sudden penetration step at a given, stationary force. This phenomenon is caused by the initiation of plastic deformation [27] or due to fracture [14]. Using the resulting load-penetration curve, the hardness, the Young's modulus as well as plastic material parameters can be derived.

Measuring the length of the emerging cracks, the equations by Lawn, Evans and Marshall [19] can be used to calculate the fracture toughness of a material. Since GaN is anisotropic, the determination of direction-dependent material parameters is rather complex. To extract fracture parameters from nanoindentation experiments, multiple measurements have to be conducted in order to gain information about the dependence on the crystal structure of the material [34].

### Indenter Shapes

In nanoindentation experiments various indenter tip shapes can be used. Common types are three- and four-sided pyramids with various indenter angles, cones or spheres. The indenter geometry has a huge influence on the material response during the nanoindentation experiments [13, 20].

In the current thesis, simulations and experiments using a Berkovich tip are considered exclusively.

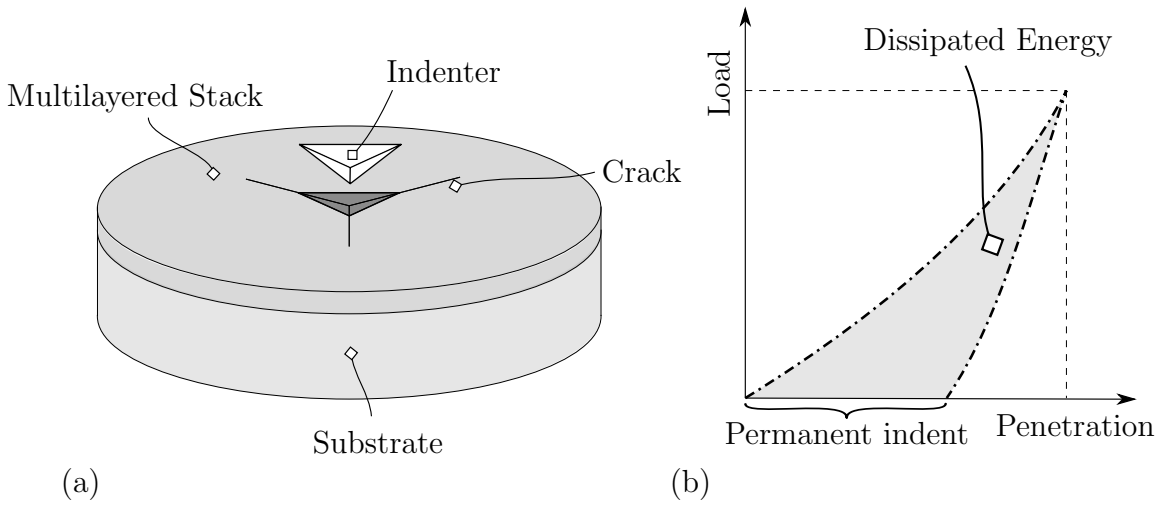


**Figure 1.2:** (a) Schematic representation of a nanoindentation experiment with a Berkovich indenter tip. (b) Typical resulting load-penetration curve.

The Berkovich indenter tip is a three-sided pyramid with a half angle of 65.3°. In Figure 1.3(a) a geometric representation of a Berkovich indenter tip is shown. Its base area is an equilateral triangle leading to the three-folded symmetry of the Berkovich indenter. It is commonly used for nanoindentation testing because it is rather unproblematic to be shaped to a sharp point, in contrast to the four-sided Vickers indenter. This ensures a much better monitoring of the indenter tip during the nanoindentation experiments. The very tip of the indenter is not perfectly sharp, but exhibits a tip radius of about 50 nm-100 nm [5].

A diamond Berkovich indenter, as shown in Figure 1.3(b), is favourable for testing brittle materials with high hardness. Due to the large included angle the influence of friction during the IIT is minimised. Diamond is often used as an indenter material because of its very high hardness, well known mechanical material parameters and the high wear resistance [5, 9].

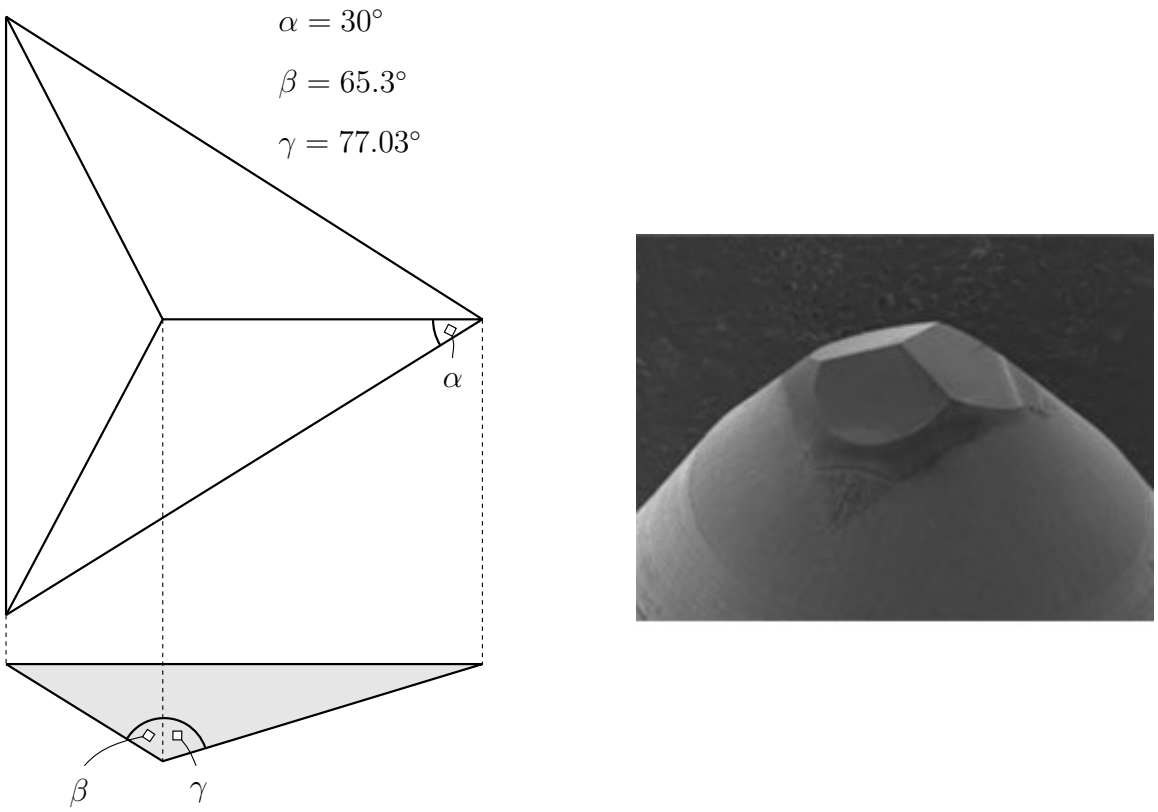


(a) (b)

**Figure 1.3:** (a) Geometric representation of a Berkovich indenter tip including relevant angle specifications. (b) Microscope image of a diamond Berkovich tip, taken from [32].

### 1.2.2 Experimental Data from KAI

Since the FEM simulations model an experimental set-up, they should portray the physical behaviour of the system to a certain extent. In order to validate the simulations and evaluate their quality, nanoindentation tests have been carried out to compare the results. All IIT experiments have been performed at the KAI GmbH, Villach. The sample used in the experiments is a 1.8 µm thick $Al_xGa_{1-x}N$ heterostructure on a $\langle 111 \rangle$ Si substrate, as described in [28].

P. Hoffmann [11] has received load-penetration data for various indentation depths up to 0.365 µm, using both a Berkovich as well as a conospherical indenter tip. Since cracks often occur only at higher indentation depths, new experiments have been

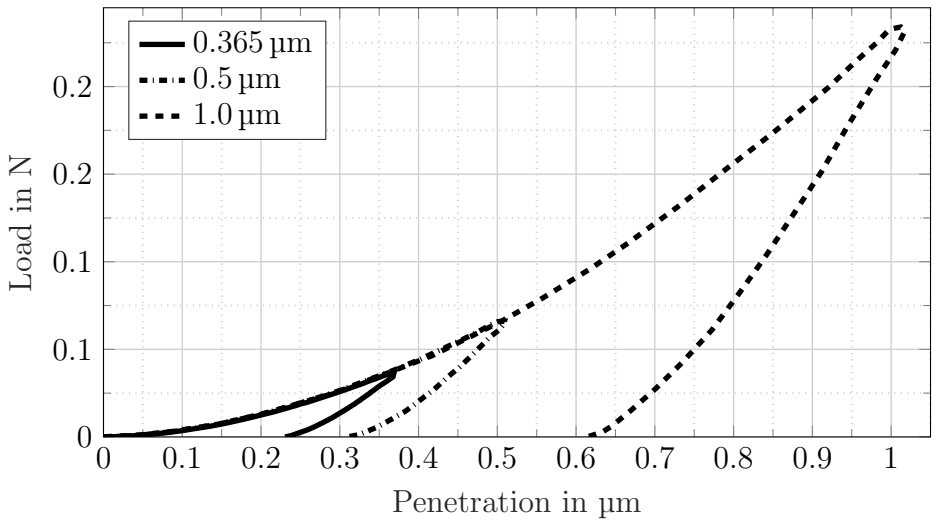


**Figure 1.4:** Experimental load-penetration curves for indentation depths of 0.365 µm, 0.5 µm and 1.0 µm, a courtesy of KAI GmbH, Villach.

conducted in March 2018 in order to support this thesis. Therefore experiments have been carried out with indentation depths of 0.35 µm, 0.4 µm, 0.5 µm, 0.6 µm, 0.8 µm and 1.0 µm using a Berkovich indenter. Each of these IITs with a specific depth has been performed five times. For all those experiments load-penetration curves as well as optical microscope images of the residual indent and the occurring cracks have been provided. In Figure 1.4 the experimental load-penetration curves for three IITs are shown. In contrast to the observations in the thesis in [11] for smaller indentation depth, there are no visible pop-in events in the load-penetration curves. Figure 1.5 depicts an optical microscope image of various indents with different indentation depths. A scale of 100 µm is pictured. Multiple residual imprints and cracks are visible. An imprint resulting from the penetration up to 1.0 µm is magnified by a factor of 5 and displayed in the centre of the picture. The indents show various forms of cracks, but most commonly radial cracks originating from the indenter edges. In the magnified area three large cracks can be observed, one of which emanates slightly next to the edge of the indent.

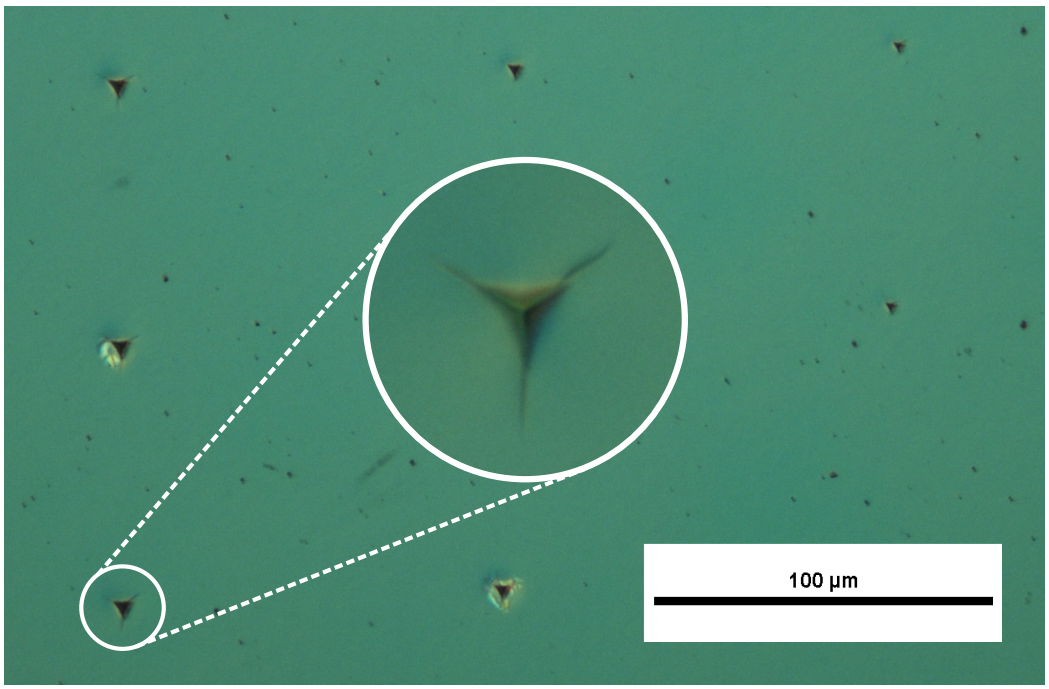


**Figure 1.5:** Optical microscope image of various indents in an $Al_xGa_{1-x}N$ on Si wafer, a courtesy of KAI GmbH, Villach. An imprint resulting from the penetration of 1.0 µm is magnified by a factor of 5.

In addition to these results, *NanoVision* (Agilent Technologies Inc., Palo Alto, CA, USA) measurements, a high-resolution surface profiling technology, were used to scan the surface after the indentation process [1]. This has been done for an imprint arising from a 1.0 µm indentation.

Due to the production process and the lattice mismatch between the layers, stacks usually exhibit significant residual stresses. The biaxial stresses in the stack shown in Figure 1.6(a) have been investigated and measured in [29] using an ion beam layer removal method in combination with micro-cantilever measurements and Finite Element simulations. In Figure 1.6(b) the resulting stress profile in the heterostructure is shown.

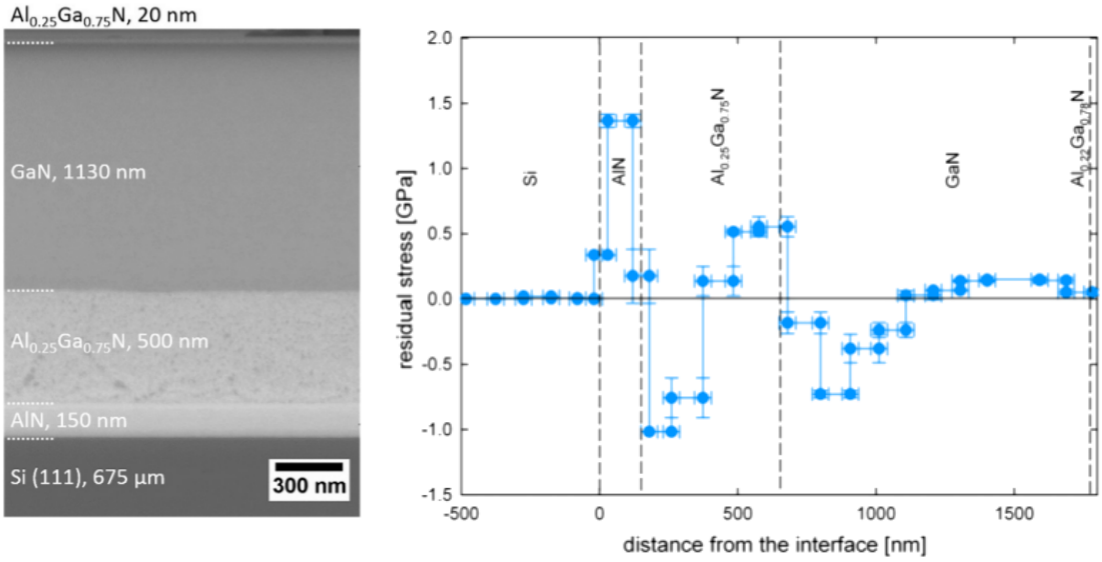


(a) (b)

**Figure 1.6:** (a) Multilayered $Al_xGa_{1-x}N$ heterostructure on a ⟨111⟩ Si substrate, used in the experiments and simulations. (b) Experimentally evaluated residual stress distribution in [29].

## 1.3 Literature Overview

In this section a brief overview of selected literature related to the topics of this thesis is given.

First of all, literature has been reviewed that deals with the formation of cracks during indentation testing in brittle materials.

J. Hagan and M. Swain [8] focused on the emergence of radial and lateral cracks. It is stated that half-penny cracks nucleate from plastic deformation, due to piling up of dislocations on two intersecting slip planes or the presence of sub surface flaws. This indicates that the plastic deformation in nanoindentation experiments has an influence on the crack formation. In [31] Y. Tang et al. have used experiments as well as analytic and numerical calculations, proclaiming that the crack emerges directly under the plastic zone growing in radial direction and furthermore upwards during the unloading of the material.

In a few articles similar FEM models, as used in this thesis, have been employed. They have focused on modelling nanoindentation experiments in brittle materials using cohesive zone elements in combination with an isotropic J2 plasticity model.
In [13], [15] and [20] the fracture toughness and the different crack shapes have been object of research. It has been shown, that nanoindentation simulations can be used to accompany and support the fracture toughness measurements. Furthermore, it has been reported that the interaction between the elastic and plastic material response has a vast influence on the crack formation and final crack shape. The shape of the indenter has been found to affect the crack formation and propagation.

I. Ratschinski et al. [25], [26] and [27] have observed the formation of cracks and dislocations in {0001} GaN bulk crystals during nanoindentation experiments using a Vickers and Berkovich indenter.
Dislocations have been reported to occur for even very small indentation depth, indicating early plastic deformation. The orientation of the indenter has no big influence on the slip planes and directions. Cracks have occurred only for higher indentation loads, depending strongly on the indenter shape and orientation. If the edges of the Berkovich tip are aligned with the prismatic cleavage planes, three radial cracks propagate from the indenter edges outwards. If the Berkovich indenter and the prismatic crack planes deviate, the radial cracks are diverted. Using a Vickers indenter tip, up to four radial cracks emerge, getting aligned with the prismatic crystal planes while growing. Beyond that, lateral cracks have been reported for indentations using a Vickers tip.

## 1.4 Scope of the Present Thesis

The present thesis deals with the non-linear FEM simulation of nanoindentation experiments in GaN on Si substrate using a Berkovich indenter tip. The main aspect

is the modelling of crack emergence and propagation in Gallium Nitride, taking into account the non-linear effects of crack formation and anisotropic plasticity.

In Chapter 2 an overview on the theoretical background is given. First the mechanical characteristics of GaN and its crystal structure is examined. Thereby the main focus is on the anisotropic plastic deformation and, in particular, on the fracture behaviour. Furthermore an introduction to fracture mechanics, focusing especially on cohesive zone methods, is given. The different crack systems emerging in GaN using a Berkovich tip are briefly outlined.

Chapter 3 focuses on the Finite Element modelling, describing the approximations and assumptions as well as all used modelling approaches. Mainly the concepts of the modelled anisotropic plasticity and crack formation are described. Similarities and differences to the models in the literature, presented in Chapter 1.3 become clearly. Additionally, the set-up of the two- and three-dimensional FEM models is presented and explained in this section.

Chapter 4 presents the simulation results of the 2D and 3D models. After looking at the load-penetration response and the stress state during the indentation, the crack formation and propagation is studied in detail. Special focus lays on the influence of fracture strength and toughness as well as the residual stresses.

Finally, Chapter 5 gives a summary of the major results obtained within this work and provides a short outlook on possible future investigations addressing unresolved issues that emerged during this work.

# Chapter 2

# Theoretical Background

## 2.1 Mechanical Characteristics of Gallium Nitride

In this section an overview of the mechanical behaviour of single crystal Gallium Nitride is given.

### 2.1.1 Crystal Structure of Gallium Nitride

A crystal is constructed by the repetition of identical clusters of atoms, forming the crystal lattice. Depending on the shape of this lattice, a unit cell is formed, defined by the primitive axes. Some materials show randomly orientated unit cells in their crystal lattice, diverging in size and orientation, whereas others show a single crystal structure. A single crystal structure is filled by the duplication of the unit cell, performing suitable translation along, or rotations around the primitive axes. The crystalline structure remains unchanged over the whole material [4, 17].
Gallium Nitride is predominantly crystallising in the Wurtzite structure. It consists of two compounds, Gallium and Nitrogen, arranged in a separate hexagonal close-packed sub lattice, respectively [22]. In this hexagonal crystal structure the axial direction of the unit cell column is called as c-axis. There are three $a_i$-axes (for $i = 1, 2, 3$)

perpendicular to the c-axis, with an included angle of 120°. The lattice constant $c$ corresponds to the height of the unit cell, constant $a$ is defined by the distance between two $a_i$-axes at the outside of a unit cell [4].
GaN shows lattice constants of $a = 3.189\,\text{Å}$ and $c = 5.185\,\text{Å}$ [22].

Within the unit cell there are certain crystallographic planes, which can either be basal, prismatic, or pyramidal. These are in connection with plasticity and fracture. The planes and directions in the hexagonal structure are labelled using Miller-Bravais indices. Planes are described by using braces, e.g. $\{0001\}$, directions by chevrons, e.g. $\langle 0001 \rangle$. The digits, describing crystal planes, correspond to the reciprocal ratio of the position of the point, where the planes intersect the axes, compared to the lattice constants. If the plane does not touch an axis, the digit in the index is 0. Crystallographic directions start in the bottom centre of a unit cell and describe the direction vectors [17].
Figure 2.1 shows schematics of hexagonal unit cells of GaN. The a-axes correspond to the $1, 2, 3$ axes, the vertical c-axis to the 4-axis. The lengths of the primitive cell are labelled with their lattice constants. Three representative types of crystallographic planes in the structure are highlighted. There is only one basal plane $\{0001\}$, two prismatic, e.g. $\{01\bar{1}0\}$ and three pyramidal planes, e.g. $\{\bar{1}2\bar{1}2\}$. Every slip plane, except for the basal, occurs six times in the unit cell, repeated in a 60° rotation pattern around the 4-axis.

### 2.1.2 Plastic Deformation of Gallium Nitride

As outlined in Section 1.1.1, the plastic behaviour of the materials in nanoindentation simulations should not be neglected. Therefore an appropriate plasticity model needs to be applied using the FEM, simulating the irreversible plastic deformations in the material.
A detailed study of the plastic behaviour in GaN has been realised by P. Hoffmann in his thesis [11].

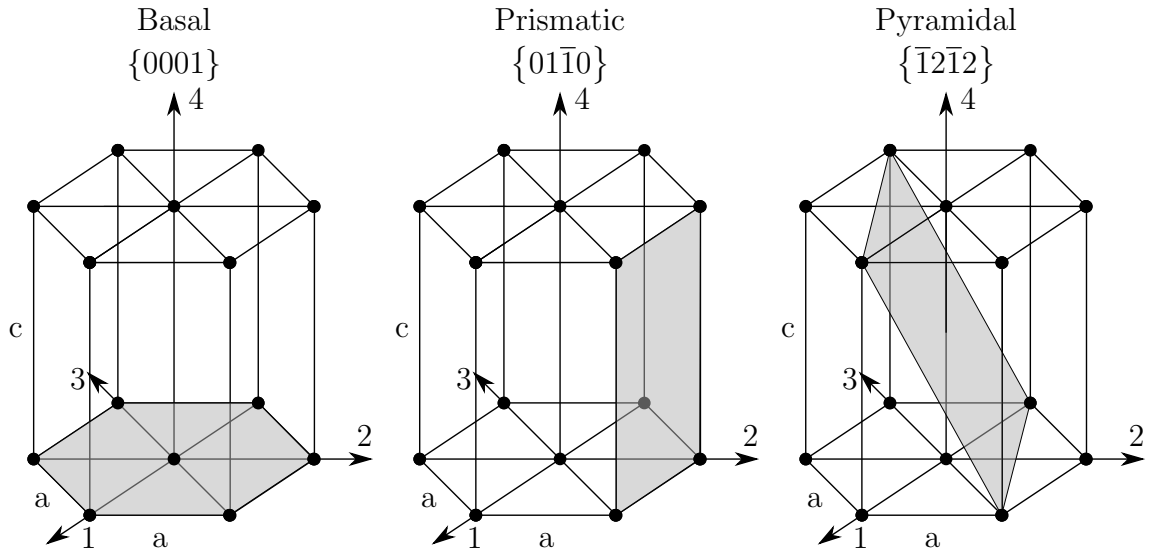


**Figure 2.1:** Crystallographic planes in a GaN unit cell. Examples of basal, prismatic and pyramidal planes are highlighted. The planes are labelled using the Miller-Bravais indices.

The yield strength in single crystals depends strongly on its lattice orientation, leading to an anisotropic behaviour. The main mechanism of crystal plasticity is the dislocation motion through the lattice on the crystallographic planes. These slip planes in conjunction with corresponding slip directions, form the slip systems in crystals. The plastic deformation is initiated if the resolved shear stress of a slip system reaches its critical value [11, 17].

For all slip systems in GaN, the critical resolved shear stress can be derived from experiments or theoretically calculated yield values. One way to empirically obtain the theoretically reached stresses, is by using the Peierls-Nabarro shear stresses. These parameters are theoretical calculations of the shear stresses required to move a dislocation through the crystallographic lattice, depending on atomic spacing. Peierls-Nabarro stresses tend to exceeded the actual reached values significantly.
The ratio between the resolved shear stress in the activated slip system and the corresponding yield strengths in a specific direction is calculated using Schmid's law. In the direction perpendicular to the basal {0001} plane a yield stress of $\sigma^{\mathrm{Y}} = 7.85\,\mathrm{GPa}$ has

been obtained from micro-compression experiments on a GaN single crystal. This is the highest yield value used in the FEM simulations in this thesis. The uniaxial yield stresses in other directions have been computed using the Peierls-Nabarro stresses in conjunction with the Schmid's factors [11].

During nanoindentation using a pyramidal indenter, slip has been found to occur widely in the basal and most commonly in the pyramidal planes [11, 25–27].

### 2.1.3 Fracture Behaviour of Gallium Nitride

The crack emergence and propagation in GaN is influenced by many different factors. Only some of the major aspects of this complex topic, that are essential for the simulation model, are considered in this section.
The indenter shape has a vast impact on the stress field in the material and therefore on the crack formation and propagation. Using different indenter tips, the crack shapes and sizes are changing [13, 27]. The cleavage planes of GaN together with the interactions of dislocations in the plastically deformed area affect the initiation of cracks. The dislocation cutting or pile-up of dislocations can lead to crack seeds and finally the formation of cracks [26]. Another cause of cracks can be a stress concentration at pre-existing flaws in the material [8].

Nanoindentation experiments in single crystal GaN, using a Berkovich or Vickers tip with an indentation orientation in the negative 4-direction, have shown that radial cracks propagate perpendicular to the $\{0001\}$ surface. The fracture occurs in the prismatic $\left\{1\bar{2}10\right\}$ or $\left\{01\bar{1}0\right\}$ cleavage planes. Each of those planes occur six times in the GaN unit cell, diverging by a rotation of 60° around the 4-axis [25].
In [34] the fracture toughness, depending on the crystal orientation of GaN has been measured using nanoindentation experiments and the equations of Lawn, Evans and Marshall [19]. The lowest fracture toughness values have been reported for the prismatic planes. Even though the $\left\{01\bar{1}0\right\}$ cleavage plane possesses the lowest value,

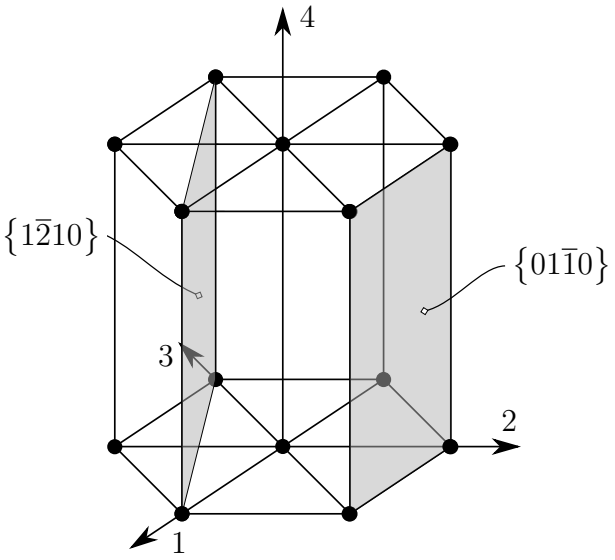


**Figure 2.2:** Prismatic crystal planes in GaN. $\{1\bar{2}10\}$ and $\{01\bar{1}0\}$ cleavage planes are the weakest in single crystal GaN, leading to cracks perpendicular to the $\{0001\}$ basal surface.

both prismatic planes show very similar fracture material parameters and differ only by about 2.5 %.

Figure 2.2 shows examples of the two prismatic crystal planes in GaN. In the considered cases, cracks occur primarily in these planes.

In [25] lateral cracks propagating almost parallel to the $\{0001\}$ surface have been observed, besides the cracks in the radial direction. This has been reported to appear using a Vickers indenter exclusively. In Figure 1.5 the cracks emerging during the experiments performed at the KAI, Villach are presented. For some indents both radial and lateral cracks are visible, despite the application of a Berkovich indenter tip. Hence, under certain circumstances, lateral cracks can emerge using a Berkovich indenter as well. Moreover, there is a possibility that these lateral subsurface cracks are caused by the delamination of layers in the stack.

## 2.2 Residual Stresses in Multilayered GaN-on-Si Structures

Due to favourable wafer production costs, GaN is often grown on a Silicon substrate using epitaxial growth. This is the deposition of a very thin GaN layer with well-defined orientation onto the single crystal Si substrate. Although GaN is grown on $\langle 111 \rangle$ Silicon, to keep the difference of the lattice constants rather low, the lattice mismatch between $\langle 0001 \rangle$ GaN and Si is still 17 %. Besides this, the difference in the thermal expansion coefficients between epitaxial GaN and the substrate plays an important role in the production process. The linear thermal expansion coefficient of GaN is $5.6 \times 10^{-6}\,\mathrm{K}^{-1}$, the value for Si only $2.6 \times 10^{-6}\,\mathrm{K}^{-1}$. This high discrepancy of material properties leads to immense residual stresses during the epitaxial growth procedure, which can eventually result in fracture and failure of the wafer.
To counteract these effects, stress management techniques have been developed to mitigate crack formation in the GaN. An efficient way to cope with high residual stresses in the wafer is to integrate multiple buffer layers. Aluminium Nitride is a suitable material due to reasonable electrical properties and a lattice mismatch of only about 3 % compared to GaN. To minimise these differences of the lattice constants, $\mathrm{Al_xGa_{1-x}N}$ layers with different amounts of Aluminium and Gallium are used. The residual stresses in the wafer can be tuned via the stack composition and thickness of the $\mathrm{Al_xGa_{1-x}N}$ layers. This way an $\mathrm{Al_xGa_{1-x}N}$ heterostructure is formed. An example of such a multi layered structure, studied in [29], can be found in Figure 1.6(a).

Despite those intense arrangements, there are still significant residual stresses in the $\mathrm{Al_xGa_{1-x}N}$ layers. Figure 1.6(b) shows the residual stress distribution over the layer heights, measured in [29]. There are tensile as well as compressive stresses up to 1.4 GPa. These high stress values are most likely to have an influence on the fracture behaviour of the GaN-on-Si wafers.

## 2.3 Fracture Mechanics

The engineering field which studies the behaviour of a cracked body and the resulting failure processes in materials and structures is called fracture mechanics. Analytical continuum mechanic methods are used to calculate the driving forces on a crack, which are compared to material parameters. To determine the material's resistance to fracture, experiments are conducted.
Using linear elastic fracture mechanics (LEFM), the material is considered purely linear elastic, assuming that the studied structures already exhibit a crack, defect, or some other sources of stress concentrations. At this points there is an increase in the crack length, if the critical stress intensity value is exceeded [2, 7].

In fracture mechanics three different crack opening modes with respect to the loading conditions are considered.
Mode I describes a tensile stress normal to the plane of the crack, Mode II a shear stress acting parallel to the crack plane and perpendicular to the crack front and Mode III a shear stress acting parallel to the plane of the crack to the crack front. In Figure 2.3 the three fracture modes are schematically depicted.

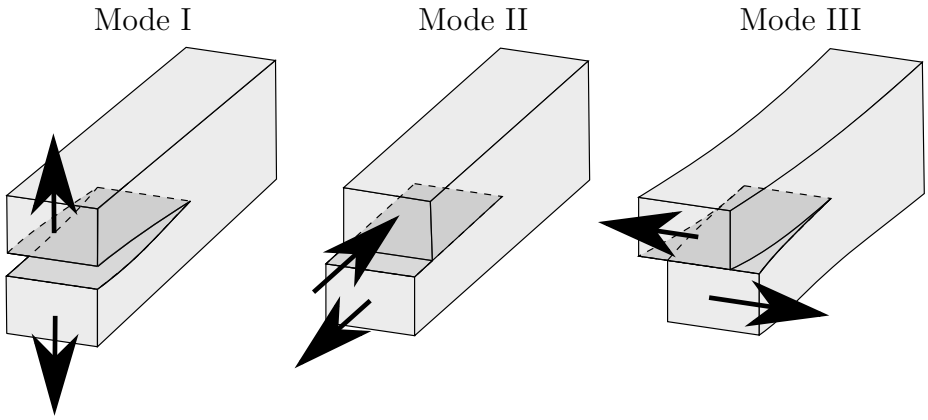


**Figure 2.3:** The three fracture modes. Mode I - Opening, Mode II - In-plane shear and Mode III - Out-of-plane shear.

In the immediate surroundings of a crack the local stress field

$$\sigma_{ij}(r,\theta) = \frac{K_{\mathrm{M}}}{\sqrt{2\pi r}} \cdot f_{ij\mathrm{M}}(\theta) \qquad \text{(for M = I,II,III)} \tag{2.1}$$

depends on the distance $r$ and the angle $\theta$ of a considered point to the crack tip. $f_{ij\mathrm{M}}$ is a function depending on the geometry, boundary conditions, the angle $\theta$ and the fracture mode M. By an asymptotic approximation of the crack tip, a stress singularity with the magnitude of $\frac{1}{\sqrt{r}}$ arises. The stress state in the vicinity of a crack is characterised by the stress intensity factor

$$K_{\mathrm{M}} = Y_{\mathrm{M}}(a) \cdot \sigma\sqrt{\pi a} \tag{2.2}$$

which depends on the crack length $a$ as well as the fracture mode. Variable $\sigma$ denotes to the nominal stress, calculated while neglecting the crack in the structure. The geometry factor $Y(a)$ depends on the geometry of the crack and the considered structure. Geometry factors are provided in diagrammatic form for many crack geometries and stress types, based on results of analytical or numerical calculations. The stress intensity factor can be compared to a material parameter i.e. the critical stress intensity factor or the material fracture toughness $K_{\mathrm{Mc}}$. If the stress intensity factor reaches its critical value

$$K_{\mathrm{M}} = K_{\mathrm{Mc}} \quad , \tag{2.3}$$

crack initiation occurs. Fracture toughness values are usually obtained using standardised experiments [7, 24].

The approach mentioned above is limited to linear elastic, perfectly brittle materials only. Since no material can withstand unlimited stresses, the stress field described by Equation (2.1) cannot be fully developed. Near the crack tip a small plastic zone is formed. If this non-elastic area reaches a critical size the LEFM no longer applies

and elasto-plastic fracture mechanic (EPFM) approaches need to be considered. The size of the plastic zone can be estimated using analytical equations [24].

### 2.3.1 Energy Based Approaches

Besides approaches considering stress fields in cracked structures, energy based methods are often used.
The following section is based on [2] and [7].

An energy consideration on fracture for linear elastic material behaviour, based on the first law of thermodynamics was established by A. A. Griffith [2]. The change in the total energy $E$ with respect to the area $A$ created by an infinitesimal crack extension

$$\frac{\mathrm{dE}}{\mathrm{dA}} = \frac{\mathrm{d}\Pi}{\mathrm{dA}} + \frac{\mathrm{d}\Gamma}{\mathrm{dA}} = 0 \tag{2.4}$$

is equal to the change in the potential energy $\Pi$ and the energy spent for the generation of the new surface $\Gamma$. The energy $\Gamma$ is dissipated, hence crack propagation is an irreversible process. According to the energy equilibrium, the equation

$$\frac{\mathrm{d}\Gamma}{\mathrm{dA}} = -\frac{\mathrm{d}(\Pi_{\mathrm{int}} + \Pi_{\mathrm{ext}})}{\mathrm{dA}} \tag{2.5}$$

must be fulfilled. The potential energy $\Pi$ therefore consists of the internal strain energy $\Pi_{\mathrm{int}}$ and the potential of the external forces $\Pi_{\mathrm{ext}}$.
In the so-called Griffith fracture criterion, the energy release rate

$$\mathcal{G} = \frac{\mathrm{d}\Gamma}{\mathrm{dA}} \tag{2.6}$$

is introduced.

It characterises the energy that is dissipated due to the formation of a new crack area. Similar to the critical stress intensity factor in Equation (2.3), a limiting value can be used to be compared to the present energy release rate in the structure. A crack criterion

$$\mathcal{G}_{\mathrm{M}} = \mathcal{G}_{\mathrm{Mc}} \qquad (\text{for M} = \text{I,II,III}) \tag{2.7}$$

can be defined for all three fracture modes, where $\mathcal{G}_{\mathrm{Mc}}$ is called the critical energy release rate. The Griffith approach indicates that a crack extension takes place, if the available potential energy is sufficient to overcome the resistance of a material. As for the fracture toughness, the critical energy release rate is often determined by using standardised experiments.

If a propagating crack tends to grow further without any increase in external loading, it is called unstable. The need of an additional increase of the external loads or other driving forces, indicates stable crack growth. The crack propagation is stable, if the total energy reaches a minimum with respect to an infinitesimal crack extension

$$\frac{\mathrm{d}^2(\Pi_{\mathrm{int}} + \Pi_{\mathrm{ext}} + \Gamma)}{\mathrm{dA}^2} > 0 \quad . \tag{2.8}$$

For linear elastic fracture mechanics G. R. Irwin derived the relation between the energy release rate and the fracture toughness as

$$\mathcal{G}_{\mathrm{I}} = \frac{K_{\mathrm{I}}^2}{E_{\mathrm{eff}}} \tag{2.9}$$

for the plane strain and plane stress state, where

$$E_{\mathrm{eff}} = \begin{cases} \dfrac{E}{1-\nu^2} & \text{plane strain} \\ E & \text{plane stress} \end{cases} \quad . \tag{2.10}$$

Here $E$ corresponds to the Young's modulus, $\nu$ is the Poisson's ratio. These correlations have been deduced for a plane stress and plane strain state, exclusively. For many structures and loading conditions, however, these assumptions are sufficient. Equation (2.9) also applies to the critical material value $\mathcal{G}_{\mathrm{Ic}}$. Equations (2.10) have been establish for isotropic materials, but are approximately modified to correspond to an anisotropic material behaviour.
In analogy, similar relations to Equation (2.9) are defined for fracture Mode II and Mode III, employing the shear modulus. These can be found in [7].

Another energy based fracture criterion is the $J$-Integral. The contour integral considers the energy directly at the crack tip. Fracture occurs, when the calculated $J$ value reaches a critical material parameter. In the LEFM, the $J$-Integral is equal to the energy release rate

$$J_{\mathrm{M}} = \mathcal{G}_{\mathrm{M}} \quad , \tag{2.11}$$

depending on the individual fracture modes. The $J$ contour integral is a commonly used parameter in fracture mechanics concerning non-linear material behaviour. By including elastic-plastic deformations to extend the fracture mechanics concepts, the $J$-Integral is an important approach in the EPFM. Concerning very complex loading- and boundary conditions, especially for three-dimensional problems, it is typically computed using numerical methods. In the presence of material non-linearities, $J_{\mathrm{M}}$ usually differs from the linear energy release rate $\mathcal{G}_{\mathrm{M}}$.

By using the Finite Element Method, the fracture mechanics considerations can be extended to a more general approach in terms of the complexity of structures, loads and boundary conditions. The following section focuses on the use of the FEM in fracture mechanics by means of cohesive interface elements.

### 2.3.2 Cohesive Zone Model

According to cohesive zone models (CZM), it is assumed that the damage process takes place in a small area ahead of the crack tip, the so–called cohesive zone (CZ). The basic concept of this modelling approach is to consider the tractions and separations between two potential crack faces, confined to planes where fracture is assumed to occur. Using the FEM, specific interface elements are commonly utilised to model fracture in ductile materials, ceramics, fibre-reinforced composites and especially along interfaces between two materials. The complicated fracture process inside the cohesive zone is condensed into interface elements of initially vanishing thickness, where the damage process is supposed to take place.
The main advantage of this model is its capability to predict crack emergence and propagation without the need of an initial crack. However, using a cohesive zone model, the direction or area of the crack growth needs to be known in advance. Utilising the CZM, the following assumptions should apply. The cohesive zone is small compared to the crack size and the dimensions of the structure. The material behaviour is constant, independent of the external loads and the position of an element in the cohesive zone or the propagating crack. The crack faces seamlessly join each other at the end of the cohesive zone [7, 18].

In the constitutive model the cohesive tractions are related to the separation of two opposing crack fronts in a *traction-seperation* law. Using a bilinear CZM, this relation reads

$$t^{\mathrm{n}} = K^{\mathrm{n}}\delta^{\mathrm{n}} \cdot (1 - D^{\mathrm{n}}) \quad , \tag{2.12}$$

where $t^{\mathrm{n}}$ are the normal cohesive tractions and $\delta^{\mathrm{n}}$ the normal crack front separations. The normal cohesive stiffness

$$K^{\mathrm{n}} = \frac{t_{\mathrm{c}}^{\mathrm{n}}}{\delta^*} \tag{2.13}$$

is related to the maximum normal cohesive traction, or fracture strength, $t_{\mathrm{c}}^{\mathrm{n}}$, and the normal crack front separation at the maximum normal traction, $\delta^*$. The damage parameter

$$D^{\mathrm{n}} = \begin{cases} 0 & \delta_{\max}^{\mathrm{n}} < \delta^* \\ \left(\frac{\delta_{\max}^{\mathrm{n}} - \delta^*}{\delta_{\max}^{\mathrm{n}}}\right)\left(\frac{\delta_{\mathrm{c}}^{\mathrm{n}}}{\delta_{\mathrm{c}}^{\mathrm{n}} - \delta^*}\right) & \delta^* \leq \delta_{\max}^{\mathrm{n}} \leq \delta_{\mathrm{c}}^{\mathrm{n}} \\ 1 & \delta_{\max}^{\mathrm{n}} > \delta_{\mathrm{c}}^{\mathrm{n}} \end{cases} \tag{2.14}$$

depends on the maximum normal crack front separation attained in deformation history $\delta_{\max}^{\mathrm{n}}$ and the normal crack front displacement at complete debonding $\delta_{\mathrm{c}}^{\mathrm{n}}$. Damage initiation starts ($D^{\mathrm{n}} > 0$), if the cohesive traction reaches its maximum. The material is considered to be failed ($D^{\mathrm{n}} = 1$), if the separation reaches the critical value, $\delta_{\mathrm{c}}^{\mathrm{n}}$.
The aforementioned equations follow the implementation in ANSYS [3].

Due to the relevance for the problem in this thesis but without loss of generality, the equations in this section consider fracture Mode I only. Corresponding equations relating to Mode II and Mode III can be found in [7] and [18].

In Figure 2.4 a bilinear traction-seperation law is shown. The normal interface traction is shown over the normal crack front separation. Path ⓐ shows the behaviour of the loading of an undamaged material. If a damaged interface is unloaded and loaded again, the tractions follow a path, as exemplarily pictured in ⓑ.

The damage process at the interface leads to a dissipation of energy. The dissipated energy due to crack formation per crack area, corresponds to the critical energy release rate $\mathcal{G}_{\mathrm{Ic}}$. This critical material parameter can be obtained using $K_{\mathrm{Ic}}$ for linear elastic

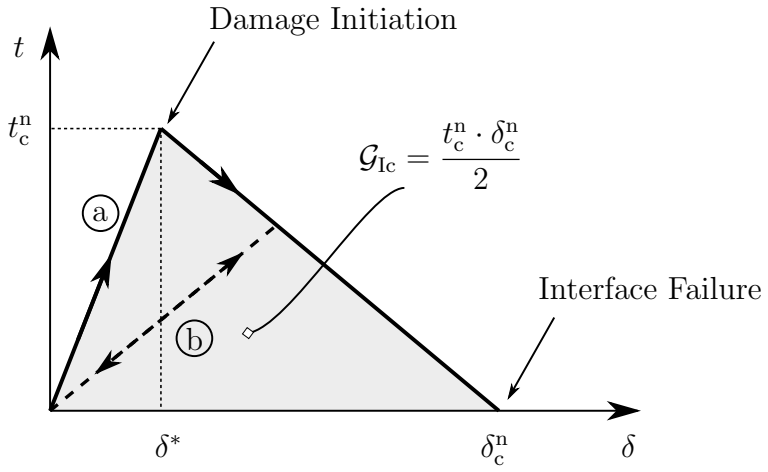


**Figure 2.4:** Bilinear traction-seperation law corresponding to fracture Mode I. The area under the curves is equivalent to the critical energy release rate $\mathcal{G}_{Ic}$. ⓐ loading path of initially undamaged interface, ⓑ loading- and unloading path for a partially damaged material.

and $J_{Ic}$ for elasto-plastic problems, respectively [18]. The area under the traction-seperation law is equivalent to the critical energy release rate and needs to conform to

$$\mathcal{G}_{Ic} = \int_0^{\delta_c^n} t^n(\delta^n)\, \mathrm{d}\delta^n \quad . \tag{2.15}$$

By using a bilinear cohesive material law, Equation (2.15) simplifies to

$$\mathcal{G}_{Ic} = \frac{t_c^n \cdot \delta_c^n}{2} \quad . \tag{2.16}$$

Using the size of the failed area, the overall dissipated energy can be calculated. In [3], [7] and [18] various other shapes of traction-seperation laws can be found.

An appropriate initial normal cohesive stiffness $K^n$ (for $D^n = 0$) needs to be chosen due to numerical reasons. If the stiffness is to high ($K^n \to \infty$), convergence problems can occur. A very low initial stiffness leads to a postponed damage onset, which can

cause inaccurate structural response due to the amount of additional elastic strain energy stored in the CZ elements. Therefore a specific finite $K^{\mathrm{n}}$ needs to be chosen. The initial cohesive stiffness is described using $t_{\mathrm{c}}^{\mathrm{n}}$ and the interface stiffness factor

$$\alpha = \frac{\delta^*}{\delta_{\mathrm{c}}^{\mathrm{n}}} \quad . \tag{2.17}$$

Using the bilinear CZM the three independent material parameters $t_{\mathrm{c}}^{\mathrm{n}}$, $\delta_{\mathrm{c}}^{\mathrm{n}}$ and $\alpha$ need to be given. The relationship between $t_{\mathrm{c}}^{\mathrm{n}}$ and $\delta_{\mathrm{c}}^{\mathrm{n}}$ can be calculated using Equation (2.16) [3].

Figure 2.5 shows a schematic picture of a crack opening profile along an interface under Mode I loading. In the elastic zone, no damage arises, hence the separations are fully reversible. The separation in the elastic zone should be small in order to keep the artificial elastic strain energy low. The process zone, $L_{\mathrm{CZ}}$, is the area, where degradation of the interface takes place. This section is also referred to as the cohesive zone. If the separations reach $\delta_{\mathrm{c}}^{\mathrm{n}}$, the interface cannot sustain any more forces and the material is considered to be fractured.

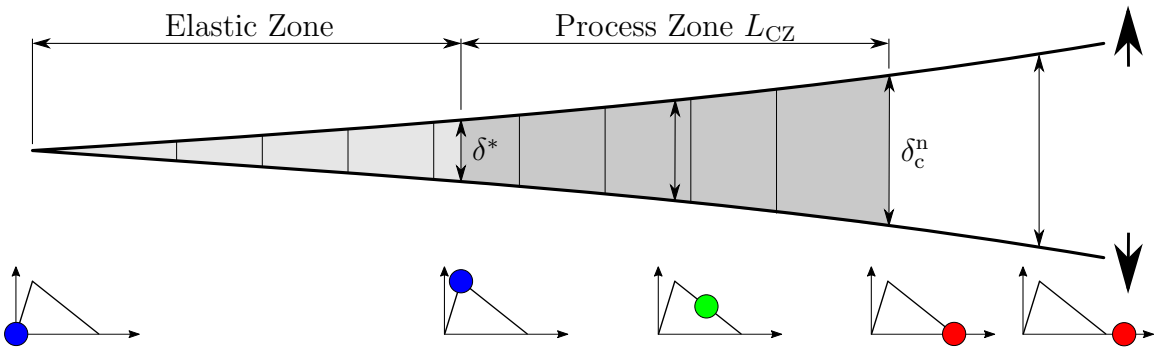


**Figure 2.5:** Sketch of a crack opening along an interface under Mode I loading. Damage at different points is depicted by a schematic traction-separation curve underneath. The elastic zone (reversible separation), the process zone $L_{\mathrm{CZ}}$ (partly damaged interface) and the cracked material ($\delta^{\mathrm{n}} > \delta_{\mathrm{c}}^{\mathrm{n}}$) are shown.

In continuum mechanics material fracture along an interface occurs continuously. Using CZ elements within the FEM the crack propagation increment is assumed as sharp discontinuity. Due to this reason and the need of a small CZ compared to the overall crack size, specific demands on the interface element size need to be made. In the process zone $L_{\mathrm{CZ}}$ a certain amount of elements should be located [18].
In [20] an estimation of the length of the process zone is given, reading

$$L_{\mathrm{CZ}} \approx \frac{E \cdot \delta_{\mathrm{c}}^{\mathrm{n}}}{t_{\mathrm{c}}^{\mathrm{n}}} \quad . \tag{2.18}$$

Since the estimation is used for isotropic materials, the specific elastic and fracture parameters need to be chosen on the basis of the direction of the crack front, in case of an anisotropic material behaviour.

**Viscous Regularization**

A high fracture strength and low fracture toughness can lead to numerical convergence problems. This issue was addressed by Y. F. Gao and A. F. Bower in [6], leading to the *viscous regularization*. A small viscosity is introduced in the cohesive zone constitutive equation. The normal cohesive tractions $t^{\mathrm{n}}$ are enhanced by adding a viscous damping term

$$\widetilde{t^{\mathrm{n}}} = t^{\mathrm{n}} + \zeta \cdot \frac{\mathrm{d}\Delta^{\mathrm{n}}}{\mathrm{dt}} \tag{2.19}$$

where $\zeta$ corresponds to the damping coefficient featuring the physical unit of a dynamic viscosity, $\Delta^{\mathrm{n}}$ to the ratio of $\delta^{\mathrm{n}}$ to $\delta^{*}$ and $t$ to the time [3]. This damping leads to a supplementary dissipation of energy, which can lead to the stabilisation of crack growth and better convergence of the simulation. Since this damping is physically not meaningful, the energy dissipated due to viscous regularization needs to be small compared to the dissipation as a result of fracture. The parameter $\zeta$ has to be chosen low enough to ensure this, but on the other hand sufficiently high to have a positive

effect on the convergence behaviour of the simulation. Viscous regularization introduces a certain time dependency in the FEM model. The time step size has an effect on the simulation results and is correlated with the damping coefficient [6].

**Fracture Strength Reduction**

Considering Equations (2.16) and (2.18) as well as a constant critical energy release rate and Young's modulus, a linear increase in fracture strength leads to a decrease of the process zone with a factor of $(t_c^n)^{-2}$. A high fracture strength has therefore a vast influence on the required mesh size in the FEM model. In [33] A. Turon et al. have described a method of reducing the fracture strength, without a variation of dissipated energy due to fracture. The procedure is based on an artificial decrease of the fracture strength, leading to a longer process zone, while keeping the critical energy release constant. By reducing the maximum interface strength, the process zone spans more elements. Although the stresses near the crack front in the bulk material are less accurately captured, the mechanisms of energy dissipation are precisely depicted. In [33] the adequate propagation of the crack front in an elastic material, when using the fracture strength reduction has been shown.
In the nanoindentation simulation models described in [13], [15] and [20] similar approaches have been applied, while using elasto-plastic material parameters for the bulk material. It has been found that the fracture strength and the shape of the cohesive law have a negligible influence on the crack propagation and the final crack shape in nanoindentation simulations. The fracture strength reduction is a useful method limit the number of interface elements, and therefore obtain reasonable computation times, while maintaining a sufficiently accurate modelling of the dissipation mechanisms.

Figure 2.6 displays a schematic illustration of the fracture strength reduction. The area under the traction-seperation laws, corresponding to the critical energy release rate, stays constant, while modifying the fracture strength.

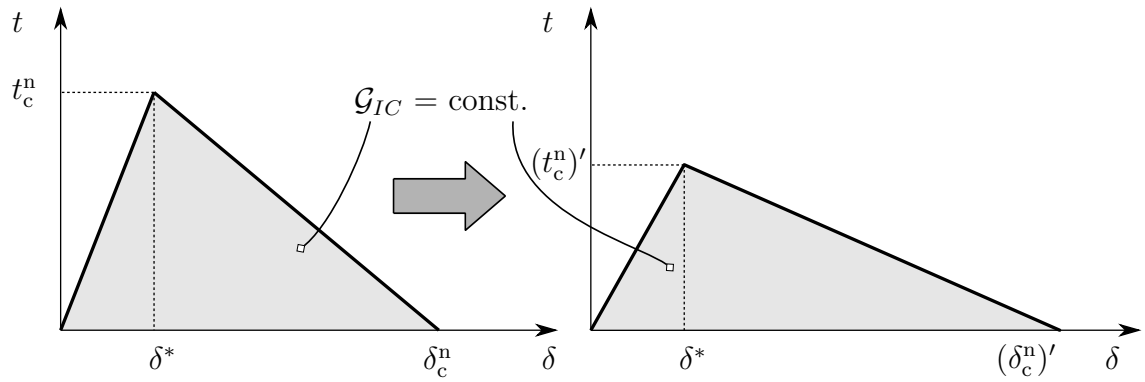


**Figure 2.6:** Schematic illustration of the fracture strength reduction. The critical traction is reduced, while the critical energy release rate stays at a constant value.

The influence of the fracture strength reduction on the FEM simulations conducted in this thesis is discussed in detail in Section 4.2.3.

### 2.3.3 Indentation Fracture Mechanics

Indentation fracture mechanics studies the fracture behaviour of materials during IIT. It is commonly used to observe and investigate the emerging cracks after the experiments and furthermore to measure the fracture toughness of materials.
While indenting, a plastically deformed region develops under the indenter area. This plastic zone is dominated by compressive stresses. In the elastic field in the immediate surrounding tensile stresses arise, which will eventually exceed the fracture strength and lead to different types of cracks. During nanoindentation experiments stresses induced by the indenter tip decrease promptly from the contact area. Therefore potential cracks are likely to be restrained [5, 20].

Figure 2.7 presents various potential crack shapes in GaN, emerging during the nanoindentation process using a Berkovich indenter.
Most of the cracks start to grow directly under the plastic zone, or set off at the indenter edges. Half-penny cracks during Vickers experiments, or quarter-penny cracks

(a) using a Berkovich tip are large cracks forming around the plastic zone, continuing in radial direction on the surface. They start during the loading of the structure and continue to grow while unloading. Smaller Palmqvist cracks (b) next to the indenter edges emerge mostly during unloading. Median cracks (c) grow form the plastic zone downwards, but are not visible on the surface. Median and Palmqvist cracks are reported to join potentially, and form a half/quarter-penny crack [5, 20]. Lateral cracks (d) emerge under the plastic zone, mostly during experiments using a Vickers indenter, but are also observed using a Berkovich tip as stated in Section 2.1.3.
The occurrence and interaction of different types of cracks is very susceptible to the loading conditions, material defects and the indenter tip shape [5, 27].

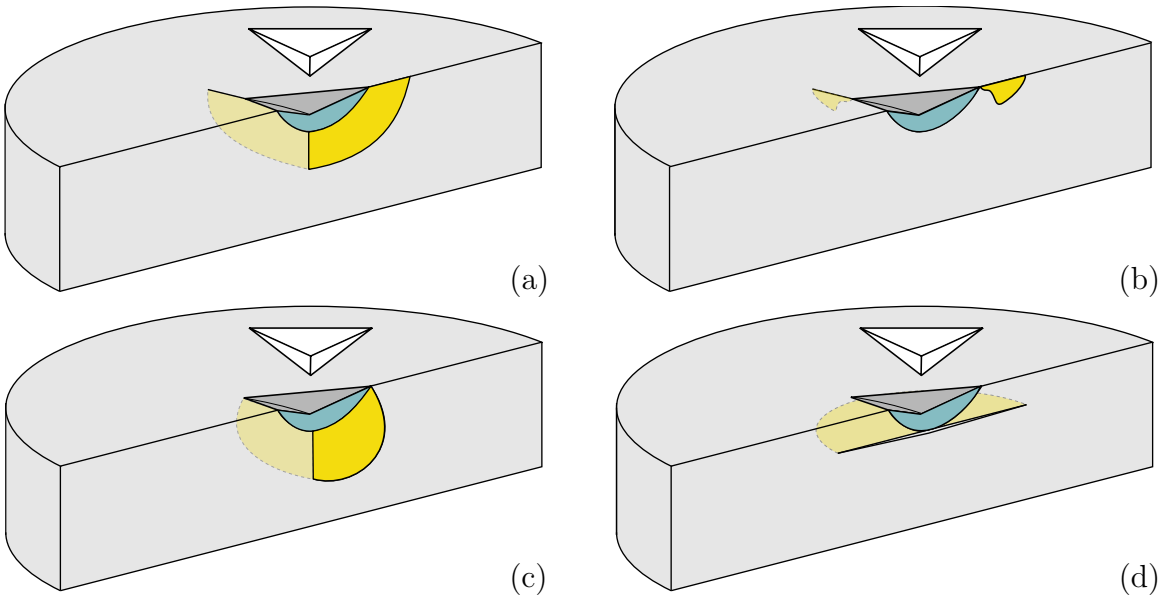


**Figure 2.7:** Sketches of common, potential crack systems, emerging during the indentation process using a Berkovich tip on GaN. (a) Quarter-penny crack, (b) Palmqvist crack, (c) Median crack and (d) Lateral crack. The plastically deformed area is highlighted in blue, the cracks in yellow.

# Chapter 3

# Finite Element Methodology

In this chapter, the Finite Element methodology underlying the nanoindentation simulation models is described.
Due to the favourable computation times and the possibility to draw first conclusions about the meaningfulness of the modelling strategy and the material behaviour, a two-dimensional (2D) plain strain FEM model is developed. Although this model is physically not reasonable, because of the incapability of representing a spatial crack system, the simulations lead to important results, that are highly relevant relating to the final three-dimensional (3D) FEM model. On the basis of the 2D model, 3D simulations are set up and used to study the behaviour of GaN layers on a silicon substrate during nanoindentation experiments and are furthermore compared to the experimental results from KAI, Villach, in order to validate the numerical model.

In all FEM simulations within this thesis, Ansys Academic Associate Mechanical release 18.2/19.0 in conjunction with the Ansys Parametric Design Language (APDL) (Ansys Inc., Canonsburg, PA, USA) is used [3].

## 3.1 Approximations and Assumptions

Since a numerical model is an abstraction of a real physical system, a range of simplifications has to be made in order to maintain a reasonable simulation effort. The objective of the simulations is to understand the behaviour of the system and its underlying causes. The challenge of numerical modelling is to find a good way of abstraction. More precisely, to capture the behaviour of the real system to a satisfying extent, but on the other hand to introduce certain approximations by neglecting insignificant factors. In the following the assumptions and approximations made in the FEM simulation models are presented.

In the simulations the unit system N, µm and s is used. Energy outputs, computed during the FEM simulations are therefore obtained in Nµm which corresponds to $1 \cdot 10^{-6}$ J.
An implicit quasistatic analysis is used to model the nanoindentation process. With the exception of the viscous regularization, no time dependent phenomena are considered. For this reason, the dwell times after loading and during the unloading of the sample are omitted, since it is postulated that the artificial viscosity has a small effect on the material behaviour. In the FEM simulation two time steps are modelled. Time step one corresponds to the penetration, step two to the unloading of the wafer structure. In order to capture the non-linear effects and achieve an appropriate time resolution of the resulting output variables, the timesteps are subdivided into smaller fractions. For most of the simulations a division of a step into 100 increments, so-called substeps, is used. In case the convergence criteria of an increment are not met after a specific amount of iterations, automatic time stepping of the Ansys solver is used, in order to refine the substeps and achieve convergence.
The coordinate origin is located in the centre of the model, directly under the indenter. The z-coordinate direction is aligned with the $\langle 0001 \rangle$ orientation of the GaN structure and the $\langle 111 \rangle$ direction of the Si. The x-y plane is located on the top of the

material stack perpendicular to the z-axis. The wafer is therefore located beneath the x-y plane, the indenter initially on top of it.

Due to the fact that the modelling of the whole sample, as tested in the experiments, would exceed the simulation capability by far, only a small fraction of the entire structure is considered. It is highly relevant that the selected boundaries do not affect the simulation results. Since the cracks reach further outwards, when penetrating deeper into the surface, the radial size of the model depends on the indentation depth. In the FEM simulations in this thesis a model radius of 25 µm is found to be appropriate. Figure 3.1(a) shows a schematic example of the experimental nanoindentation set-up. In (b) a top view of the symmetry model used in the simulations is shown. The Berkovich indenter as well as the crystal structure of GaN exhibit a three folded symmetry. Hence only a sixth of the whole geometry is modelled, as indicated in the sketches in Figure 3.1. Using a symmetrical model, special considerations must be given to the boundary conditions at the symmetry planes.

The diamond Berkovich indenter tip is assumed to be much stiffer than the other materials in the model. Therefore a rigid indenter is modelled. Moreover the small radius on the very tip of the indenter is neglected. This leads to a stress singularity directly under the contact region. The stress state in this area should be interpreted with caution.

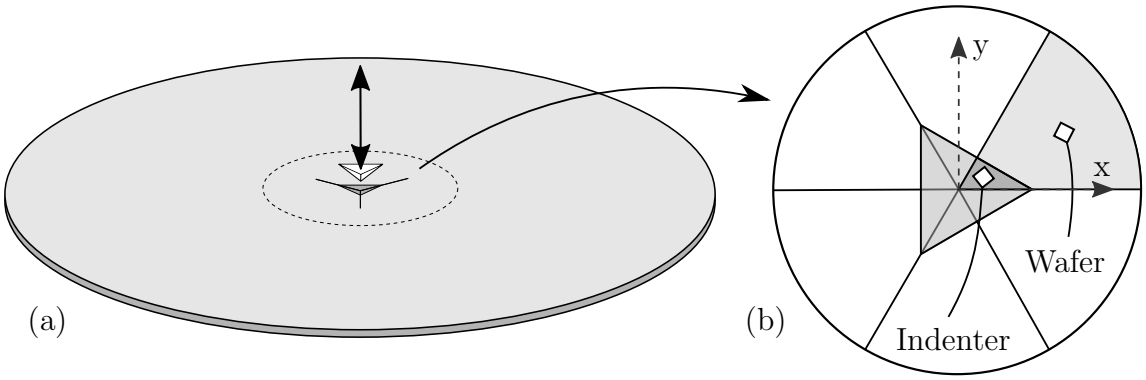


**Figure 3.1:** (a) Sketch of the experimental nanoindentation set-up. (b) Only a sixth of the geometry is modelled due to symmetry.

The simulations are performed as displacement controlled. The indentation is simulated by prescribing a translational displacement of the indenter in the negative z-direction while penetrating and reducing it to zero during the unloading load step. The displacement is applied incrementally according to the substeps.
The side faces of a Berkovich indenter include a rather flat angle, for the purpose of minimising friction. Hence frictional effects arising between the indenter tip and the wafer are neglected. This is to reduce the overall complexity of the contact modelling.

Certain requirements are put on the maximum element size due to the cohesive zone length and the non-linear contact between the indenter and the wafer. In order to get reasonable fracture results, three to five elements are placed in the process zone, depending on the used fracture strength. In the area around the contact zone, a fine mesh is used in order to get an adequate convergence behaviour and reduce contact penetration. The same element size as for the cohesive elements is applied in this area. The element size is increased in a few intervals as they approach the outside boundary of the geometric model, since the stress fields decay quickly. The interface elements follow this enlargement. For higher indentation depth, or simulations including residual stresses, where cracks are expected to be larger, the fine meshed area is adjusted accordingly. By doing so, higher computation times need to be accepted. Cracks growing in a coarse meshed region tend to be rather inaccurate.

In the first preceding thesis in [28], the material behaviour has been considered to be isotropic. Due to the crystal structure of semiconductor materials, this assumption is only a rough approximation. In [11] the model has been enhanced, featuring transversely isotropic elastic material behaviour of GaN and Si. The assumption of transversely isotropic plastic behaviour is another approximation of the hexagonal crystal structure of GaN. However the simulations in [11] have displayed good compliance with the experimental results. Silicon holds a face-centered cubic structure, and therefore cubic material behaviour but is also approximated transversely isotropic in $\langle 111 \rangle$ direction in the FEM simulations. The anisotropic plasticity of GaN is taken

into account using Hill's potential, whereas the plastic behaviour of Si is simulated using a J2 model.

In the simulations the $Al_xGa_{1-x}N$ heterostructure is approximated by using only GaN layers with an overall thickness of 1.8 µm. Therefore the stack treated in [29] is simplified. As no material data is available, it is assumed that $Al_{0.25}Ga_{0.75}N$ inhibits similar material behaviour as GaN.

During the simulations, a constant temperature at room temperature level is assumed. Therefore there is no need for temperature dependent material parameters. Since only static simulations are performed, the heat generation due to dissipative effects is not taken into account.

During nanoindentation high compressive stresses and large strains occur underneath the indenter. According to [14] phase transformations can occur in GaN under the high pressure during nanoindentation. A phase change in the materials is excluded in the FEM simulations.

Cracks are considered to emerge in the prismatic planes at the symmetry boundaries of the geometry solely. Cohesive interface elements are only placed on these surfaces. Due to this approximation only radial cracks can be simulated. These assumptions imply that the indenter edges are aligned with the prismatic planes of the GaN. As described in the literature overview in Section 1.3, cracks start to grow from the indenter edges, propagating mainly in the prismatic planes, even if the indenter and this planes initially deviate. Furthermore it is assumed that the cleavage planes of GaN and $\langle 111 \rangle$ Si are aligned.

Due to the symmetry at the cleavage planes and the structure, only fracture Mode I is considered. Therefore, critical fracture values concerning the other modes do not need to be specified. Because of the symmetry, only half of the critical energy release rate needs to be specified. This is achieved by dividing the critical separation in half. The critical energy release rate is computed using Equation (2.9). Although a elasto-plastic material behaviour is considered, the validity of the equation is assumed. In

the plastic zone beneath the indenter compressive stress emerge. Next to this area, where the cracks initiate, the material is still considered to behave elastically. Therefore the applicability of the LEFM is assumed. The plane strain case in Equation (2.10) is applied in the calculations.
The fracturing of an interface between two layers in the stack or at the substrate is not modelled. Interface failure or delamination is therefore not considered in the simulations.

## 3.2 Modelling Approaches

With regards to the modelling techniques, special focus is given to the anisotropic plasticity, the contact region between the wafer and the indenter and the cohesive interface elements.

### 3.2.1 Anisotropic Plasticity

Classic crystal plasticity modelling within an FEM simulation is computationally very complex and time consuming. Therefore Hill's plasticity theory [10] is applied to model the anisotropic plastic behaviour of GaN. Hill's criterion was originally developed for rolled steel sheets but can be adapted for a variety of applications presuming that three orthogonal planes of symmetry are preserved.

The equations in this section follow [10], the notation is adapted from [3].
In order to model the plastic deformation in a material a yield criterion, a flow rule and a hardening rule need to be defined. A yield criterion $f(\sigma, \sigma^{\mathrm{Y}})$ provides information on whether a stress state leads to a purely elastic response ($f < 0$) or causes a plastic deformation ($f = 0$). The surface defined by the yield criterion, portrayed in the stress space, is called the yield surface. If there is a plastic deformation, the flow rule connects the current stress state with the direction of the plastic strain increment. The stress cannot exceed the yield surface. If a material does not behave ideally plastic, a hardening rule needs to be defined. This rule describes the change of

the yield surface, which can be expanded (isotropic hardening) or shifted (kinematic hardening).
In the simulations in this thesis the yield criterion and the flow rule are governed by the anisotropic Hill potential. For the hardening behaviour a direction independent isotropic hardening rule is used.

Considering the specified element coordinate system, the six yield stress ratios or Hill parameters

$$\begin{aligned} R_{xx} &= \frac{\sigma_{xx}^{\mathrm{Y}}}{\sigma_0} & R_{xy} &= \sqrt{3}\frac{\tau_{xy}^{\mathrm{Y}}}{\sigma_0} \\ R_{yy} &= \frac{\sigma_{yy}^{\mathrm{Y}}}{\sigma_0} & R_{yz} &= \sqrt{3}\frac{\tau_{yz}^{\mathrm{Y}}}{\sigma_0} \\ R_{zz} &= \frac{\sigma_{zz}^{\mathrm{Y}}}{\sigma_0} & R_{xz} &= \sqrt{3}\frac{\tau_{xz}^{\mathrm{Y}}}{\sigma_0} \end{aligned} \tag{3.1}$$

are defined, where $\sigma_{ii}^{\mathrm{Y}}$ and $\tau_{ij}^{\mathrm{Y}}$ are yield stress values of the stress tensor and $\sigma_0$ is the reference yield stress. The reference value is usually chosen to be the maximum yield stress. Using six abbreviations, the so-called Hill constants

$$\begin{aligned} F &= \frac{1}{2}\left(-\frac{1}{R_{xx}^2}+\frac{1}{R_{yy}^2}+\frac{1}{R_{zz}^2}\right) & L &= \frac{3}{2}\left(\frac{1}{R_{yz}^2}\right) \\ G &= \frac{1}{2}\left(\frac{1}{R_{xx}^2}-\frac{1}{R_{yy}^2}+\frac{1}{R_{zz}^2}\right) & M &= \frac{3}{2}\left(\frac{1}{R_{xz}^2}\right) \\ H &= \frac{1}{2}\left(\frac{1}{R_{xx}^2}+\frac{1}{R_{yy}^2}-\frac{1}{R_{zz}^2}\right) & N &= \frac{3}{2}\left(\frac{1}{R_{xy}^2}\right) \quad , \end{aligned} \tag{3.2}$$

the effective Hill stress

$$\sigma_{\mathrm{eff}} = \sqrt{F(\sigma_{yy}-\sigma_{zz})^2 + G(\sigma_{zz}-\sigma_{xx})^2 + H(\sigma_{xx}-\sigma_{yy})^2 + 2L\tau_{yx}^2 + 2M\tau_{xz}^2 + 2N\tau_{xy}^2} \tag{3.3}$$

can be written in a comprehensible way. This is an extension of the von Mises (J2) criterion. The effective stress is used to define the yield function for the Hill's criterion

$$f = \sigma_{\mathrm{eff}} - \sigma_0 \quad . \tag{3.4}$$

If the effective yield stress reaches the defined reference value, plastic deformation occurs.
Using a transversely isotropic material and the stack coordinate system, the constants of the Hill yield criterion simplify to

$$N = F + 2H = G + 2H, \qquad L = M \quad . \tag{3.5}$$

The transversely isotropic plastic material behaviour is defined by the yield values $\sigma_{zz}^{\mathrm{Y}}$, $\sigma_{xx}^{\mathrm{Y}} = \sigma_{yy}^{\mathrm{Y}}$ and $\tau_{xz}^{\mathrm{Y}} = \tau_{yz}^{\mathrm{Y}}$. Using these values combined with the Equations (3.5), $\tau_{xy}^{\mathrm{Y}}$ can be calculated.

### 3.2.2 Indenter Contact

The contact between the wafer and the indenter depends on the current indentation depth and changes during the simulation process. Therefore a non-linear contact needs to be defined in the FEM models.
The following is based on the surface to surface contact definition in ANSYS [3].

The contact is specified by defining a contact and a target surface. Since the target body is suggested to exhibit a stiffer material, the rigid indenter is chosen to be the target, the wafer to be the contact surface. The Augmented Lagrangian contact algorithm is selected. If nodes between two surfaces approach each other, the normal contact pressure

$$P_{\mathrm{n}} = \begin{cases} 0 & \text{if } u_{\mathrm{n}} > 0 \\ k_{\mathrm{n}} \cdot u_{\mathrm{n}} + \lambda_i & \text{if } u_{\mathrm{n}} \leq 0 \end{cases} , \tag{3.6}$$

depending on the normal surface penetration $u_{\mathrm{n}}$ is computed, where $k_{\mathrm{n}}$ is the normal contact stiffness coefficient. The Augmented Lagrangian algorithm enhances the pure penalty method, which uses the penalty factor $k_{\mathrm{n}} \cdot u_{\mathrm{n}}$, by a Lagrange multiplier $\lambda_i$. An iterative series of penalty updates is used to determine the Lagrange multipliers.

Compared to the pure penalty method, the Augmented Lagrangian algorithm usually results in better conditioning of the stiffness matrix and is less sensitive to the user supplied contact stiffness coefficient. Large stiffness values lead to a smaller contact penetration, while convergence difficulties are likely to arise.

The surface penetration is determined on nodal points, normal to the target surface. The contact is chosen frictionless. Furthermore no damping is defined.
In Figure 3.2(a) the contact between the indenter (Target Elements) and the wafer (Contact Elements) is shown. In (b) the two surfaces are depicted in contact. A contact is detected at a node, the contact penetration $u_{\mathrm{n}}$ is calculated normal to the target surface. The normal contact pressure acts in this direction as well.

In the simulations a relative normal contact stiffness coefficient of $1 \cdot 10^3$ is used. This factor in combination with the Young's modulus of the neighbouring elements is used to define the stiffness factor of the contact elements. An absolute penetration tolerance value of 5 % of the smallest element size is applied. If the penetration exceeds this value, another iteration is enforced.

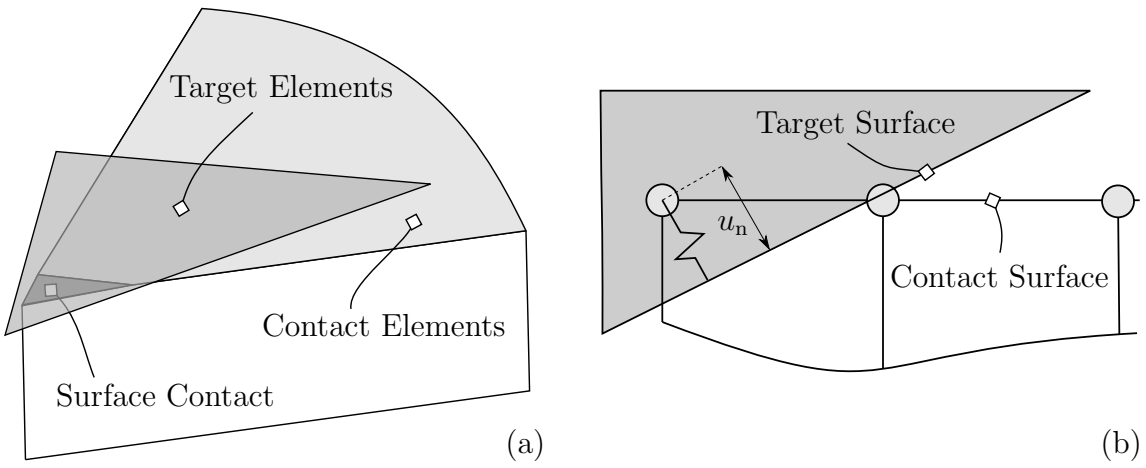


**Figure 3.2:** (a) Indenter tip in contact with the wafer. The symmetry model is shown. (b) Sketch of the surface to surface contact model.

### 3.2.3 Cohesive Zone and Symmetry Modelling

In the simulation model the cohesive interface elements are placed in the two symmetry planes of the geometry. The indenter edge is aligned with one potential crack plane. Due to the three-folded symmetry, the second crack plane is the extension of the first one. Therefore a crack may emerge and grow in both symmetry planes.
The interface elements have an initial thickness of zero and are usually placed on a surface between solid elements. Since a symmetry model is used, solid elements are only located on one side of the CZ elements. The interface nodes, that are not connected to solid elements must be provided with appropriate symmetry boundary conditions.

Due to the missing stiffness of solid elements at one side of the interface, contact constraints are placed between the nodes of the CZ elements in order to prevent penetration. The following is based on the node to node contact definition in Ansys [3]. The Augmented Lagrangian contact algorithm is selected. The CONTA178 node to node contact elements are chosen. In the simulations an absolute contact stiffness coefficient of $E_y \cdot 2.5 \cdot 10^3$ N µm$^{-1}$ is used. An absolute penetration tolerance value of 2.5 % of the crack front displacement at complete debonding $\delta_c^n$ is allowed. Hence damage of the CZ elements due to penetration is prevented.
Since no friction is employed in any of the simulations these contact elements can only transmit normal forces. Therefore the contact elements are required to be orientated perpendicular to the crack planes throughout the simulation. To ensure this, the nodes at the boundaries need to be follow the displacements of the solid element nodes in all directions but the crack opening. The nodes are coupled using equations to link the particular degrees of freedom.

## 3.3 Material Properties

In this section the material parameters used in the FEM simulations are presented and outlined briefly.
The transversely isotropic material behaviour in ANSYS is obtained by adapting a general orthotropic material model.

### Elastic Properties

The elastic parameters of GaN have been considered in more detail in [11]. In the literature a variety of experimentally obtained or theoretically calculated elasticity parameters can be found, that deviate severely. P. Hoffmann [11] has reported that the transversely isotropic parameters of R. B. Schwarz et al. in [30] have shown the best compliance with the experimental results, considering the loading- and unloading curve of the load-penetration diagrams.

The values concerning Si in the $\langle 111 \rangle$ direction correspond mainly to the transversely isotropic parameters calculated in [12], in combination with the parameters in [16], as they have been used in [11].

Table 3.1 shows the transversely isotropic elastic material parameters used to model the behaviour of GaN and $\langle 111 \rangle$ Si.

**Table 3.1:** Summary of the transversely isotropic elastic material parameters [11]. Young's moduli and shear moduli are specified in GPa, Poisson's ratios are dimensionless.

| Material | $E_x = E_y$ | $E_z$ | $\nu_{xz} = \nu_{yz}$ | $\nu_{xy}$ | $G_{xz} = G_{yz}$ | $G_{xy}$ |
|---|---|---|---|---|---|---|
| GaN | 284.4 | 160.6 | 0.212 | 0.311 | 81.4 | 108.5 |
| $\langle 111 \rangle$ Si | 169 | 187.5 | 0.182 | 0.262 | 66.9 | 57.8 |

### Plastic Properties

Similarly to the elasticity properties, the material parameters concerning the plasticity, have been adopted from [11]. The transversely isotropic yield stresses of GaN have been taken from the literature or calculated analytically. The method to obtain the transversely isotropic yield stresses from critical resolved shear stresses of the crystal systems is presented in [11].
The yield stress in z-direction $\sigma_{zz}^{\mathrm{Y}}$ is used as the reference yield stress $\sigma_0$. The Hill parameters are set in relation to this reference value. The model is using only one tangent modulus $E_{\mathrm{T}}$.

In Table 3.2 the transversely isotropic plastic material parameters for GaN are summarised.

Owing to the application of a J2 plasticity model, only one yield stress as well as a hardening parameter are needed to describe the plastic behaviour in $\langle 111 \rangle$ Si. A yield stress of $\sigma^{\mathrm{Y}} = 6.9\,\mathrm{GPa}$ is used, being in accordance with [11].
Silicon is reported to show nearly no hardening after yielding [17]. In the simulations a low, tangent modulus of $E_{\mathrm{T}} = 0.5\,\mathrm{GPa}$ is employed.

**Table 3.2:** Summary of the transversely isotropic plastic material parameters for GaN from [11].

| Yield stresses in GPa | | | |
|---|---|---|---|
| $\sigma_{xx}^{\mathrm{Y}} = \sigma_{yy}^{\mathrm{Y}}$ | $\sigma_{zz}^{\mathrm{Y}}$ | $\tau_{xz}^{\mathrm{Y}} = \tau_{yz}^{\mathrm{Y}}$ | $\tau_{xy}^{\mathrm{Y}}$ |
| 2.79 | 7.85 | 2.34 | 1.41 |
| **Hill parameters** | | | |
| $R_{xx} = R_{yy}$ | $R_{zz}$ | $R_{xz} = R_{yz}$ | $R_{xy}$ |
| 0.355 | 1 | 0.516 | 0.312 |
| Tangent modulus $E_{\mathrm{T}} = 50\,\mathrm{GPa}$ | | | |

### Fracture Mechanical Properties

The fracture parameters used in the simulations are primarily as receive from the KAI, Villach, or estimated and studied during the working process of this thesis. Fundamental estimations of the fracture toughness of the prismatic cleavage planes under Mode I loading are quoted to be around $0.4\,\mathrm{MPa}\sqrt{\mathrm{m}}$ for GaN and $0.7\,\mathrm{MPa}\sqrt{\mathrm{m}}$ for Si. In [34] much higher values up to $1.55\,\mathrm{MPa}\sqrt{\mathrm{m}}$ have been obtained for GaN. Therefore the effect of the fracture toughness on the fracture behaviour during the indentation process is studied.

Using Equations (2.9) and (2.10), the critical energy release rate of the materials can be calculated, by assuming to be in the scope of application of the LEFM. Due to the anisotropic material behaviour, the elastic constants $E_y$ and $\nu_{yz}$ are used.

Preliminary studies are carried out in order to assess the FEM input variables related to the CZM. A suitable compromise between convergence behaviour and energy considerations is made by using an artificial interface stiffness factor of $\alpha = 0.1$. The elastic energy stored in the interface elements, needs to be small compared to dissipated energy in the CZ.
A value of $\zeta = 0.075\,\mathrm{Pa\,s}$ is found to be an appropriate choice of the viscous regularization parameter.
A more precise comparison of the energies in the system is done in Chapter 4.

Table 3.3 summarises the relevant fracture parameters, used in the FEM simulations.

**Table 3.3:** Summary of the fracture parameters and the cohesive zone input.

| Material | $K_{\mathrm{Ic}}$ in $\mathrm{MPa}\sqrt{\mathrm{m}}$ | $\mathcal{G}_{\mathrm{Ic}}$ in $\mathrm{N\,m^{-1}}$ | $\alpha$ | $\zeta$ in $\mathrm{Pa\,s}$ |
|---|---|---|---|---|
| GaN | 0.4 | 0.53718 | 0.1 | 0.075 |
| $\langle 111 \rangle$ Si | 0.7 | 2.80337 | 0.1 | 0.075 |

Fracture strength parameters for GaN and Si have been provided by the KAI, Villach and have been reported to reach up to 7 GPa. Since a reduction of the fracture strength is of advantage in general, its impact on the model behaviour is studied.
A high fracture strength leads to the need of very small elements at the interface. In Figure 3.3 the influence of the fracture strength on the length of the cohesive zone in GaN is pictured. The length is computed using Equation (2.18). In this calculation the critical energy release rate of GaN as well as the in-plane Young's modulus is applied. It is visible that an increase in fracture strength leads to a vast decline of the cohesive zone length. A fracture strength of 7 GPa results in $L_{\mathrm{CZ}} = 0.006\,24\,\mu\mathrm{m}$, whereas a reduction to 1 GPa leads to $L_{\mathrm{CZ}} = 0.305\,58\,\mu\mathrm{m}$. Placing three elements in the cohesive zone using a fracture strength of 1 GPa yields a required element size of approx. 0.1 µm. As a consequence of 7 GPa fracture strength, a minimum element size of about 0.002 µm is demanded. In a 3D model of the present simulations this would exceed reasonable computation times by far. A fracture strength reduction is therefore an inevitability in order to run rational simulations. The influence of the fracture strength on the model is presented in Section 4.2.3.

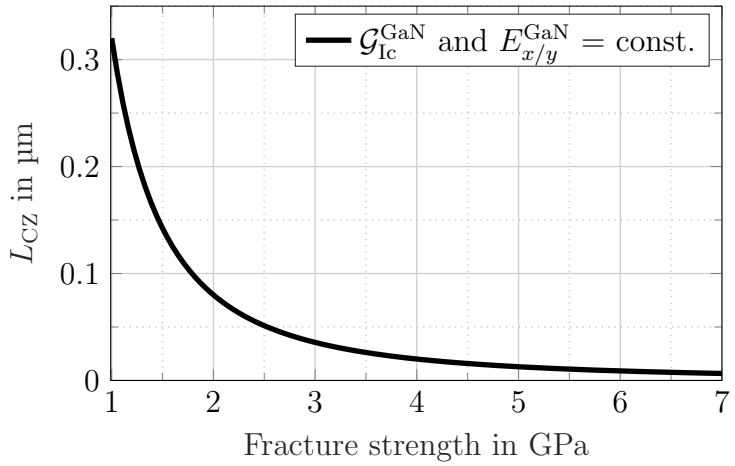


**Figure 3.3:** Influence of the fracture strength on the length of the cohesive zone in GaN. A high fracture strength leads to a small $L_{\mathrm{CZ}}$ and therefore to the need of very small elements.

## 3.4 2D Nanoindentation Model

In this section the 2D Finite Element model is explained in more detail.
Since a plain strain model is used, the crack system and the stress state caused by the Berkovich indenter cannot be depicted correctly. However a 2D model gives the possibility to obtain preliminary results allowing to draw important conclusions concerning further model development. Due to the low number of degree of freedoms, compared to a three dimensional model, a much smaller element size can be used.

In Figure 3.4(a) the geometry used in the 2D simulations is pictured. Because of the symmetry, only one half of the whole geometry is modelled. The symmetry line and the crack plane comply with the z-axis. The $^1/_2$ model is a square with a side length of 25 µm. This size is found to be appropriate for all 2D simulations within this thesis. The boundary conditions have no influence on the stress state and the cracks under

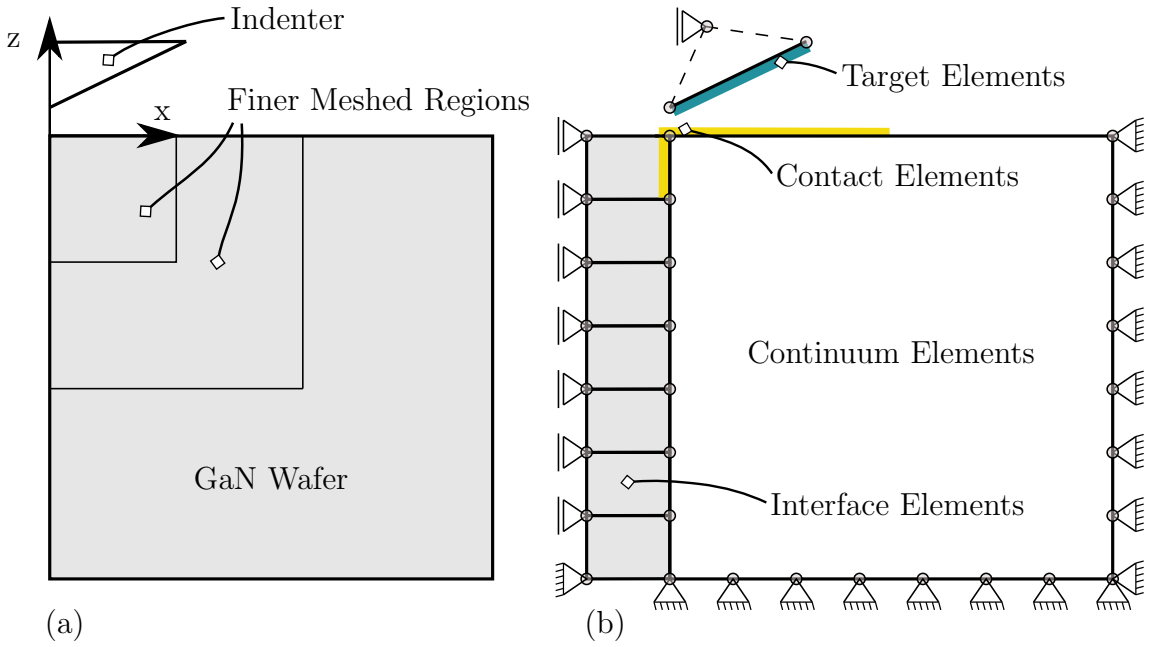


**Figure 3.4:** (a) Geometry of the 2D model. The z-axis complies with the symmetry line. (b) Boundary conditions and used element types. Blue corresponds to target elements, yellow to contact elements.

the indenter. The fine meshed region under the indenter and next to the crack has a side length of 0.8 µm, including an element edge length of 0.005 µm. The element size is enlarged five times by a factor of three, approaching the outer boundaries. Figure 3.4(b) shows a sketch of the used elements and boundary conditions in the model. The wafer is modelled using 4-node fully integrated quadrilateral elements (PLANE182) applying the plain strain option. In the cohesive zone elements (INTER202) with an initial thickness of zero are placed. For visualisation purposes the elements are depicted with a certain thickness. All degrees of freedom at the bottom nodes of the wafer as well as the radial boundaries are constrained. Due to the symmetry of the problem, the nodes at the interface, that are not connected to the plane strain elements, need to be constrained in x-direction. To prevent penetration contact elements (CONTA178) are placed between the nodes of the CZ elements. In order to guarantee a constant orientation of these contact elements the nodes at the interface are coupled in the z-direction. The indenter is meshed with traget elements (TARGE169), which are marked blue in the schematic depiction. The top surface of the wafer consists of 2-node contact elements (CONTA171), highlighted in orange. In case of high penetration depths the target elements may get in contact with the crack plane. Therefore contact elements are placed on this surface as well, as indicated in the sketch.
To model the indenter movement, the displacement of a master indenter node is prescribed in negative z-direction. Every other target node follows this translation. The whole wafer is considered to be composed of GaN only. No Si substrate is modelled. All the 2D simulations are run without the incorporation of residual stresses.

In the simulations a direct solver with predictor and line-search options is used. Geometrical non-linearities are taken into account.
The displacement as well as the reaction force at the master indenter node is captured during the simulation. This data is used to obtain the load-penetration curve. The elastic and plastic strain energies and furthermore the energy variables in the cohesive zone are monitored for further post-processing.

## 3.5 3D Nanoindentation Model

Based on the knowledge obtained from the 2D simulations, a 3D FEM model is set up. Using this model, the spacial crack system as well as the stress state under the indenter can be simulated. The predicted results of the numerical model can be compared to the nanoindentation experiments. Due to the highly increasing number of degrees of freedom, the amount of elements in these simulations is limited. Therefore, larger elements have to be used compared to the 2D simulations.

Figure 3.5(a) shows the schematic three-dimensional geometry of the symmetry model. The height and radius of the model are chosen to exhibit a size of 25 µm. As for the 2D model this value is found to be adequate for the simulated indentation depths. In the sketch the finer meshed regions are indicated. Directly under the indenter a mesh size of 0.1 µm is used. Approaching the boundaries of the model the element side length is increased, similar to the 2D model. The size of the fine meshed region varies, depending on the expected crack size. In Figure 3.5(b) the side view, Figure 3.5(c) the top view of the boundary conditions and the used elements in the 3D simulations are pictured. The GaN layers and the substrate are modelled using fully integrated, linear tetrahedral continuum elements (SOLID185). Hexahedral elements are found to induce a highly distorted mesh which leads to convergence problems. In the potential crack planes interface elements (INTER205) with an initial thickness of zero are placed. For visualisation purposes the elements are depicted with a certain thickness. All degrees of freedom at the bottom nodes of the wafer as well as the radial boundaries are constrained. Symmetry boundary conditions are applied on the outside nodes of the interface elements. As described for the 2D model, contact elements (CONTA178) need to be placed between the nodes of the interface elements. To guarantee their orientation, the interface nodes are coupled to each other in the z-direction as well as in the direction parallel to the crack faces. Only a crack opening perpendicular to the symmetry planes is permitted. The indenter is meshed with

target elements (TARGE170), which are marked blue in the Figures 3.5(b) and (c). All indenter nodes are coupled to one master node. The top surface of the wafer consists of linear contact elements (CONTA173), highlighted in orange. In case of high penetration depths the target elements may get in contact with the crack planes. Therefore contact elements are placed on these surfaces as well, as indicated in the sketch.

The indenter penetration is prescribed using a displacement of the master node in the

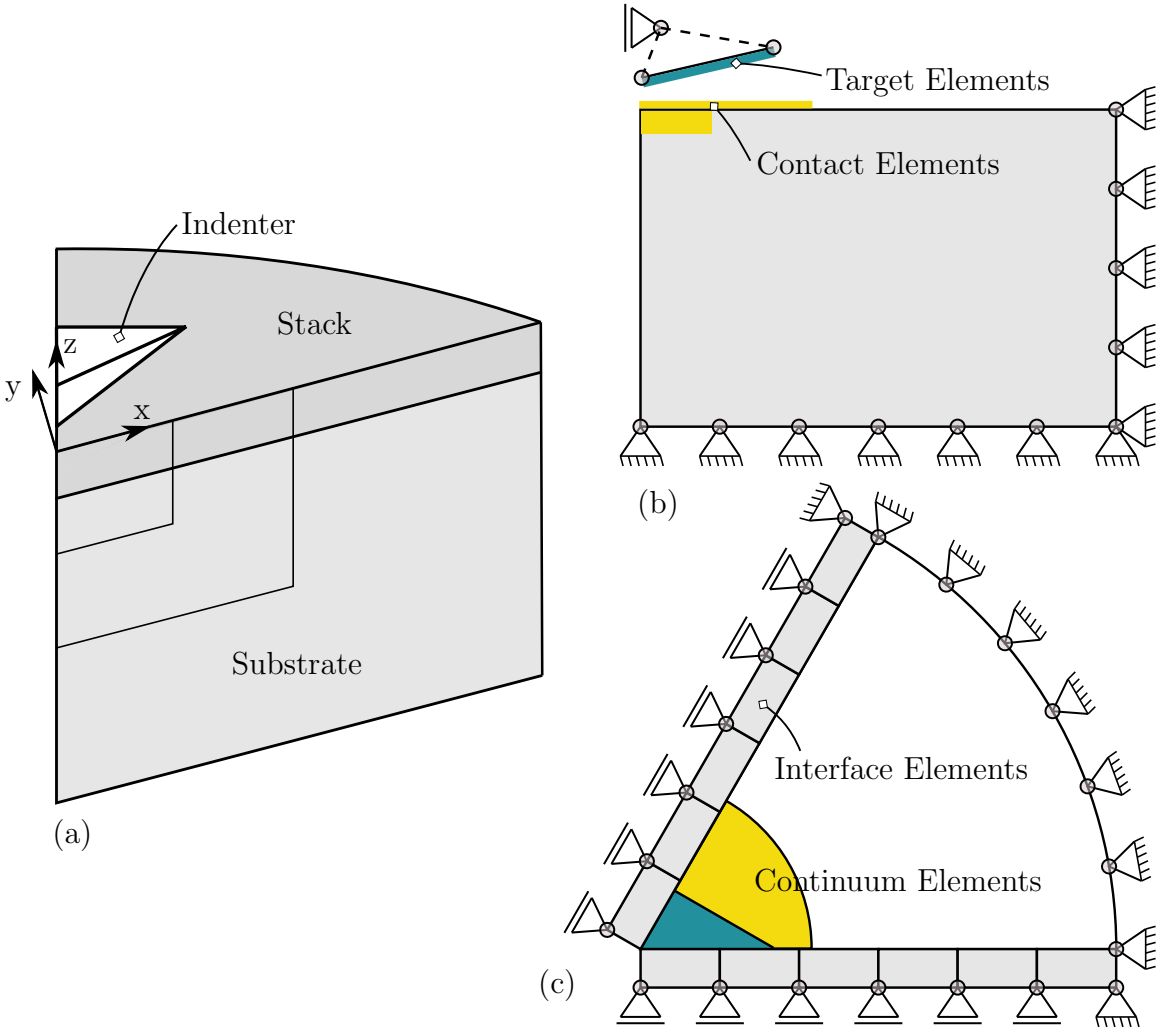


**Figure 3.5:** (a) Geometry of the 3D $^1/_6$ symmetry model. Side view (b) and top view (c) of the boundary conditions and used elements in the 3D simulations. Blue corresponds to target elements, yellow to contact elements.

negative z-direction. The simulation settings as well as the post-processing routines remain unchanged compared to the 2D model.

### 3.5.1 Residual Stress State

The residual stresses in the wafer are modelled using an initial time step. Although GaN is considered as the only top material on the Si substrate, a number of layers have to be applied in the FEM model, in order to simulate the inhomogeneity of the residual stresses in the heterostructure. In these layers a biaxial stress state in the x-y plane is assumed, as obtained in [29].
If stresses are applied directly in an initial load step, no additional strain energy is stored in the material after the computation of an equilibrium state in Ansys. Therefore, the stresses are approximated by deploying an initial elastic strain state. To calculate the strains

$$\varepsilon_{xx} = \frac{1}{E_x}(\sigma_{xx} - \nu_{xy} \cdot \sigma_{yy}) \tag{3.7}$$
$$\varepsilon_{yy} = \frac{1}{E_y}(\sigma_{yy} - \nu_{xy} \cdot \sigma_{xx}) \quad ,$$

the Young's moduli $E_x$, $E_y$ as well as the Poisson's ratio $\nu_{xy}$ are used. For a biaxial stress state $\sigma_{\text{res}} = \sigma_{xx} = \sigma_{yy}$ and the transversally isotropic material behaviour $E = E_x = E_y$, these equations simplify to

$$\varepsilon_{\text{res}} = \frac{\sigma_{\text{res}}}{E_{\text{biax}}} \quad , \tag{3.8}$$

where

$$E_{\text{biax}} = \frac{E}{(1 - \nu_{xy})} \quad . \tag{3.9}$$

Four different stack designs are simulated. In Figure 3.6 the residual stress distribution over the layer heights are shown. Stack (a) shows a uniform tensile stress in the whole GaN layer. In (b) the stresses in the GaN layers are similar to [29] as pictured in Figure 1.6. To study the interaction between tensile and compressive stresses, the two Test Stacks 1 and 2 are applied. Under a stress free top both exhibit a layer under tensile and compressive stresses of 1 GPa. In Test Stack 1 the compressive layer is directly under the top layer, in Test Stack 2 the tensile stress layer.

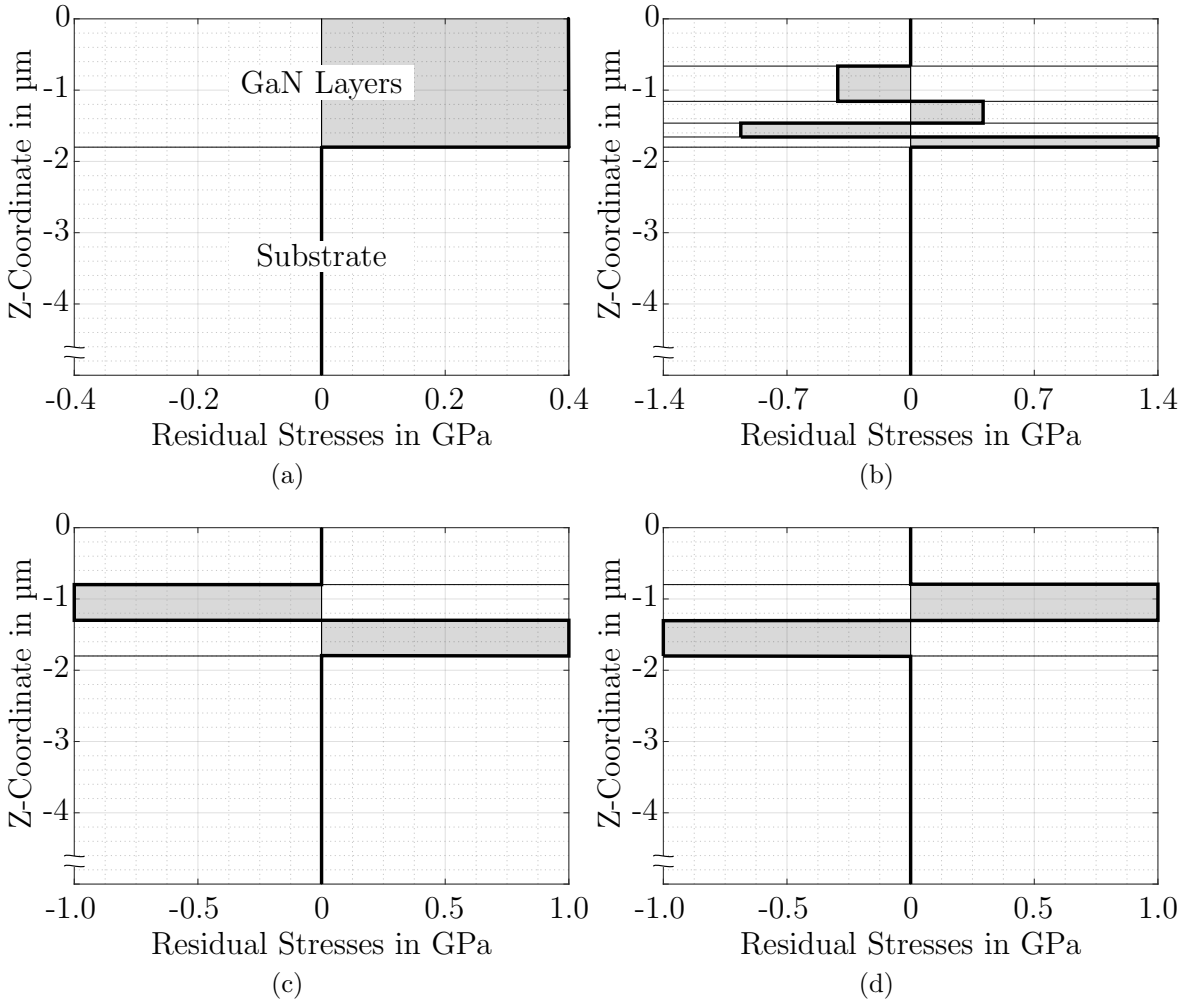


**Figure 3.6:** Residual stresses over the stack height in a 1.8 µm GaN stack on a Si substrate. (a) 0.4 GPa in the GaN layer, (b) Stack considered in [29], (c) Test Stack 1, (d) Test Stack 2.

# Chapter 4

# Simulation Results and Discussion

In this chapter the simulation results are presented and discussed.
First the main results of the two-dimensional computations are described and the most important findings pointed out.
The main focus is on the three-dimensional simulations, especially the crack emergence and its underlying causes. Various influences on the model, such as the indentation depth, material parameters and residual stresses are studied.

Due to the symmetry conditions the reaction forces and calculated energies obtained in the simulations do not represent the full model. All results presented in the following sections refer to the entire geometrical model. Since a plane strain model is used in the 2D simulations, the results are related to unit thickness.

## 4.1 2D Nanoindentation Model

Preliminary studies are conducted in order to assess a variety of simulation parameters. An indentation depth of 0.365 µm is used in the 2D simulations in the following sections.
Different solvers and solver settings are applied in order to compare the computation

times. The direct solver showed advantages concerning speed and convergence performance. Using an iterative solver leads to convergence issues due to the non-linearities in the model and therefore to prolonged simulations and inaccurate results. The arising energy due to the viscous damping in the cohesive zones exceeds the dissipated energy due to crack formation while using an iterative solver. Furthermore, the use of predictor and line-search algorithms shows reduced calculation times.
An interface stiffness factor of $\alpha = 0.1$ (see Equation (2.17)) is found to be suitable. Up to the point, where a crack starts to emerge, a certain amount of elastic energy is stored in the CZ elements. As the crack grows further this energy is slowly decreased. The maximum elastic cohesive energy is 4.75 % of the dissipated energy in the interface elements.
An estimation of the viscous regularization parameter $\zeta = 0.075\,\mathrm{Pa\,s}$ turned out to be reasonable. An in-depth consideration of energies in the interface elements is given in Section 4.1.1.
The possibilities of the fracture strength reduction are considered in detail in Section 4.1.2. Due to the use of 2D elements, the number of degrees of freedom is comparatively low, giving the opportunity to use a fracture strength up to 4.5 GPa, placing three 2D elements with a side length of 0.005 µm in the CZ. The influence of the reduction of the fracture strength is pointed out.

Due to the plain strain assumption, the results cannot be compared to experimental data. However, the simulation parameters and settings obtained during the 2D simulations are maintained in the 3D model.

### 4.1.1 Structural Response

#### Load-Penetration Curve

In Figure 4.1 the predicted load-penetration curve of the indentation is shown. The deviation of the loading and unloading curves indicates the dissipation of energy

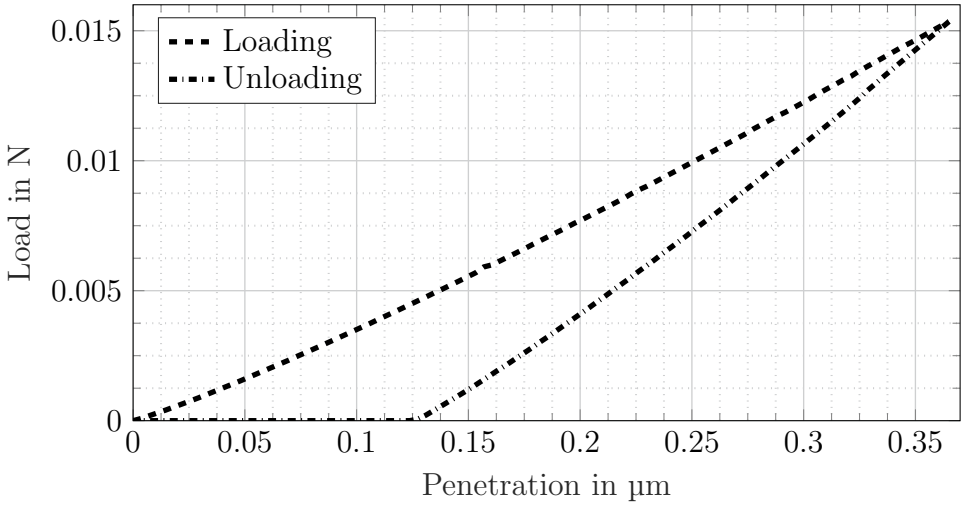


**Figure 4.1:** Predicted load-penetration curve for an indentation depth of 0.365 µm. Energy dissipation is indicated by deviating loading and unloading curves.

during the indentation process. The results are obtained using a reduced fracture strength of 0.9 GPa. Even though the simulations do not replicate a real experimental set-up, the curves show resemblances with the experimental results in Figure 1.4. Due to the plane strain assumption and the modified stress state, the slopes of the curves are different, compared to the experiments. During unloading the reaction force reaches zero at 0.1237 µm. This is the residual indentation depth, implying plastic material deformations. The load-penetration curve does not provide detailed information about the mechanisms behind the energy dissipation. Therefore further energy considerations need to be made.

### Energy Considerations

To evaluate the dissipated energy, as a result of different mechanisms, the energy in the system is examined in more detail. In Figures 4.2 and 4.3 the predicted energies are plotted against the simulations step time. The step time 0-1 corresponds to the penetration, time 1-2 to the unloading of the structure. The variable $W_{\mathrm{Ext}}$ corresponds to the applied external energy due to the indentation, $W_{\mathrm{El}}$ is the elastic

strain energy in the continuum elements and $W_{\mathrm{Pl}}$ the plastic dissipated energy. In the cohesive zone, $W_{\mathrm{CZ}}$ is dissipated due to crack growth, $W_{\mathrm{Reg}}$ is the dissipated viscous damping energy owing to the viscous regularization.

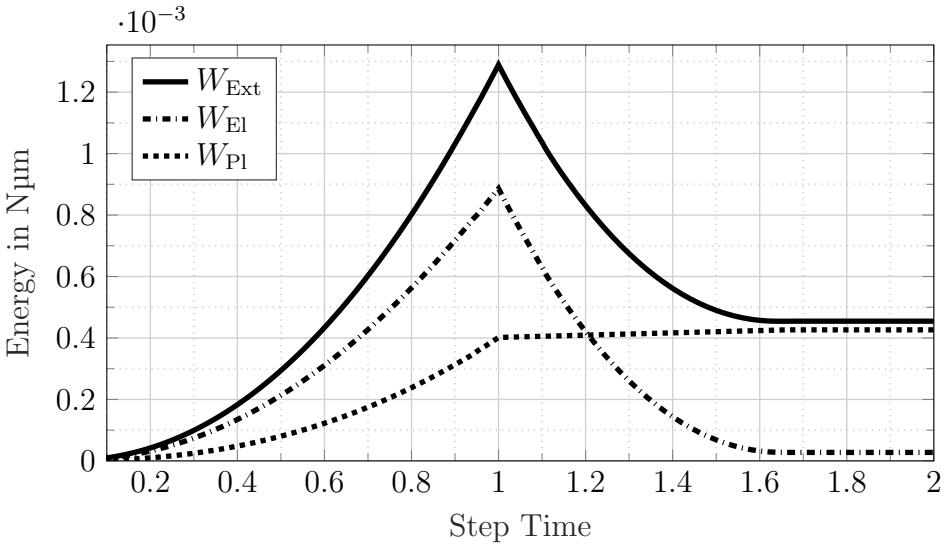


**Figure 4.2:** Applied external energy $W_{\mathrm{Ext}}$, elastic strain energy $W_{\mathrm{El}}$ and plastic dissipated energy $W_{\mathrm{Pl}}$ during the indentation. Step time 0-1 corresponds to the penetration, 1-2 to the unloading of the structure.

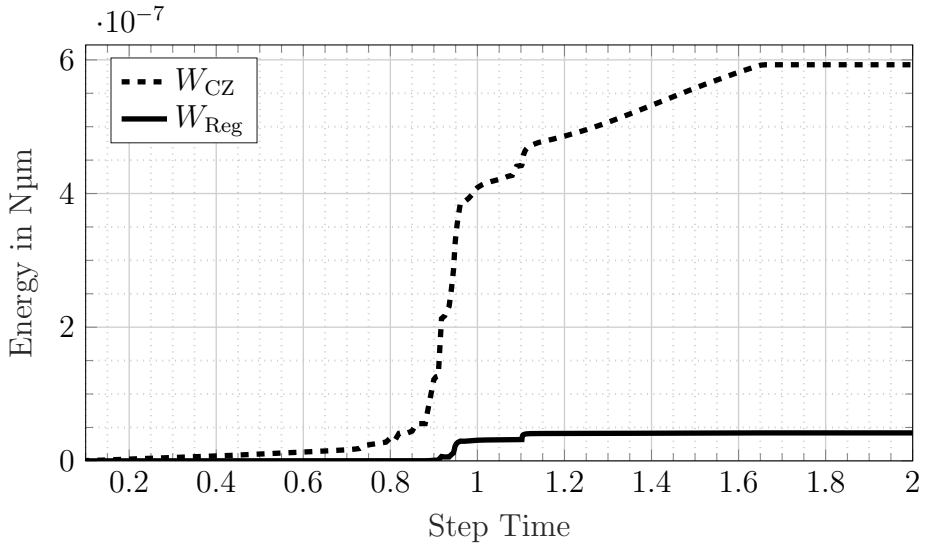


**Figure 4.3:** Dissipated energy due to fracture $W_{\mathrm{CZ}}$ and viscous regularization $W_{\mathrm{Reg}}$. Step time 0-1 corresponds to the penetration, 1-2 to the unloading of the structure.

The external applied energy raises as the indentation depth is increased. This energy is either stored elastically or dissipated due to plastic deformation or fracture. During the unloading of the wafer, the external energy decreases with the reversible elastic strain energy. Since there is an energy dissipation, the external work is not fully recovered. It is visible that there is some residual elastic strain energy in the model after the end of the simulation. The plastic dissipated energy increases slightly during the unloading. In Figure 4.3 it is notable that the energy dissipated due to fracture is three orders of magnitude smaller compared to the plastic strain energy at the end of the indentation. Therefore the dissipated energy in the cohesive interface elements does not contribute a notable deviation of the loading and unloading curve in the load-penetration diagram. The divergence is primarily because of the plastic dissipation.

At a step time of about $t = 0.86$ there is a vast increase of dissipated energy in the CZ. At this point a large crack emerges. It is notable that the crack continues to grow during the unloading, since $W_{\mathrm{CZ}}$ increases. At a step time of about $t = 1.65$ all energies stay constant. Here the indenter loses the contact to the wafer.

The dissipated energy due to the viscous regularization, in order to stabilise crack growth, stays rather small compared to the fracture energy ($\approx 7\,\%$). The ratio of the maximum elastic energy in the interface elements to the fracture energy is even smaller ($\approx 4.75\,\%$). The parameters defining the elastic stiffness and the amount of regularization are therefore estimated acceptably.

The unloading behaviour of the structure is mainly defined by the elastic material parameters. The unloading curve in Figure 4.1 is therefore mostly governed by the elastic material response.

A variety of simulations are run with different fracture strength values from 0.9 GPa up to 7 GPa. Using a fracture strength over 4.5 GPa leads to less than three elements in the CZ and possibly inaccurate solutions. Nevertheless the use of a fracture strength of 1 GPa and higher prevents any crack emergence. This phenomenon is studied in the next section.

### 4.1.2 Fracture Strength Evaluation

The following results are obtained using a fracture strength of 0.9 GPa. Figure 4.4 shows the normal cohesive tractions at the interface from the surface of the wafer to a depth of -4 µm. Figure 4.4(a) corresponds to an indentation depth of 0.073 µm, Figure 4.4(b) to 0.146 µm, Figure 4.4(c) to 0.256 µm and Figure 4.4(d) to the final penetration of 0.365 µm. Directly under the indenter very high tensile tractions occur. This is due to the stress concentration at the indenter tip. Below this region high compressive stresses arise. Compressive tractions ($< 0$) are not shown in the plots. Inside this compressive zone the yield criterion is met, so a plastically deformed area

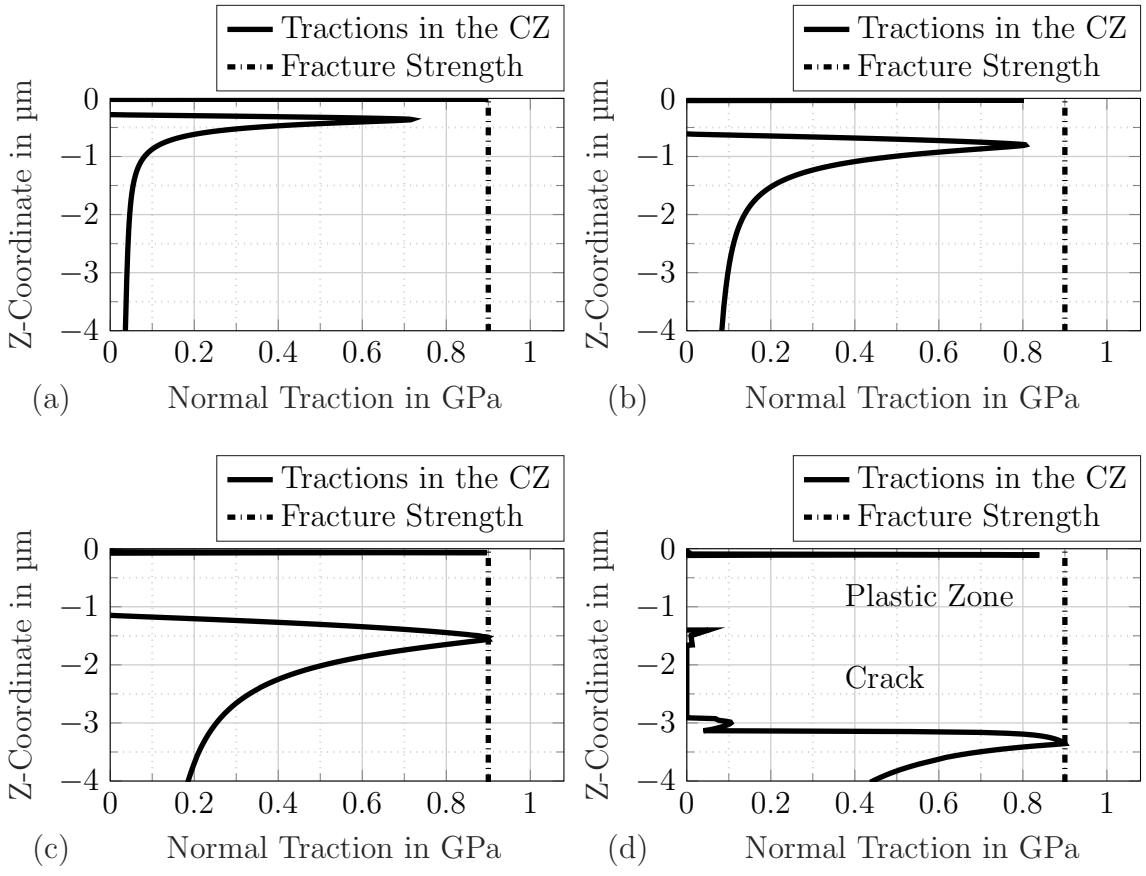


**Figure 4.4:** Normal tractions at the interface *including* cohesive elements for indentation depths of (a) 0.073 µm, (b) 0.146 µm. Crack emergence starts in (c) 0.256 µm and continues in (d) 0.365 µm.

develops. Right below this zone the highest tensile tractions occur. As the indenter penetrates further (Figure 4.4(b)), the plastic zone and the tensile tractions extend deeper into the material until the fracture strength is reached (Figure 4.4(c)). During further indentation a crack is formed. In Figure 4.4(d) the crack as well as the plastic zone are labelled. After fracturing the material cannot sustain any more tensile tractions, so they decrease to zero.

In Figure 4.5 the normal tractions at the interface from the surface of the wafer to a depth of -4 µm are shown. These results are obtained from simulations without the modelling of interface elements. Therefore, no crack emergence and propagation is possible. Figure 4.5(a) and Figure 4.5(b) show the same behaviour as in the

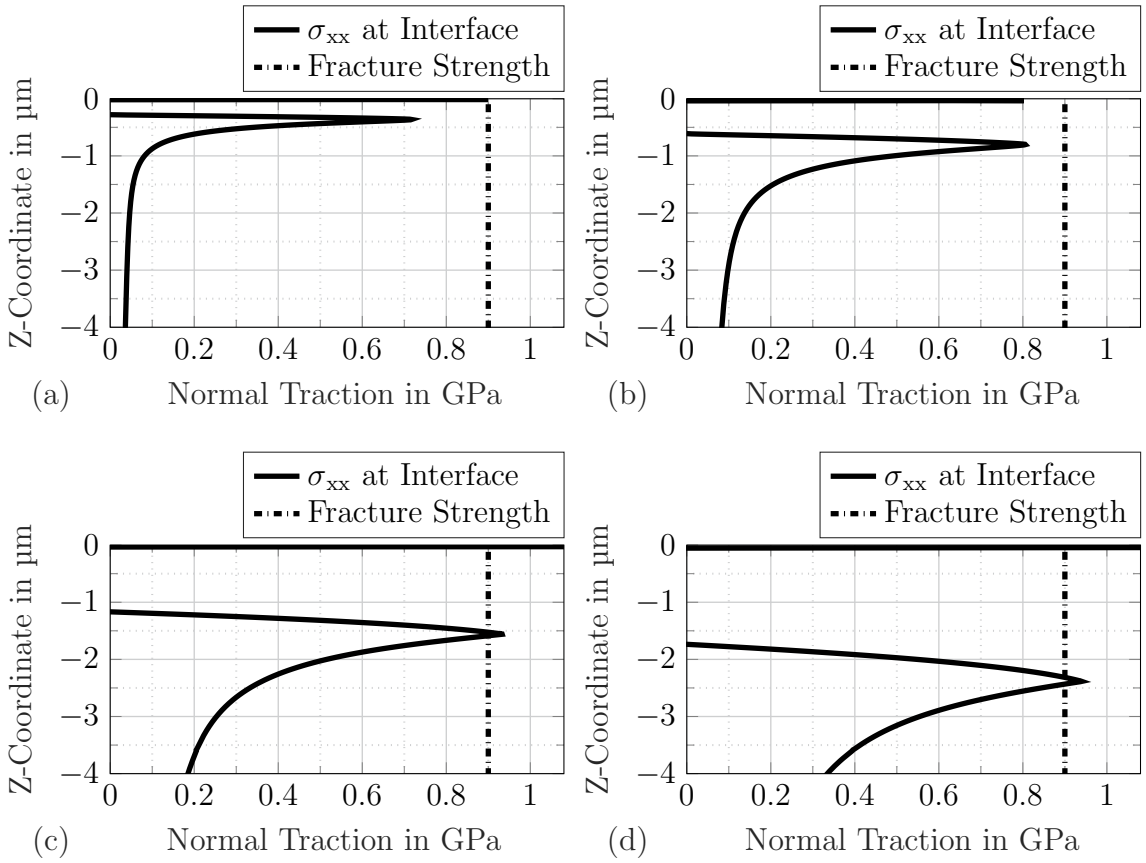


**Figure 4.5:** Normal tractions at the interface *without* cohesive elements for indentation depths of (a) 0.073 µm, (b) 0.146 µm, (c) 0.256 µm and (d) 0.365 µm.

calculations including cohesive interface elements. In Figure 4.5(c), as the indentation depth is increased, the tractions would exceed the fracture strength of 0.9 GPa. Since no crack is modelled, the tractions are not limited. Figure 4.5(d) shows the final simulation results. Even if the indentation depth is increased further, the tractions do not increase further. For higher indentation depths no rise in the maximum interface tractions is found.

Therefore, in order to model a crack in the material using the CZM, the fracture strength needs to be reduced. Simulations with various fracture strength values showed an alteration in dissipated energy in the CZ of only about 8 %. In [20] an estimation of a reasonable reduced fracture strength is given as $t_c^n \approx 0.2 \cdot \sigma_{yy}^Y$.

The crack starts to grow directly below the plastic zone, if the fracture strength is reached and continues to grow in the negative z-direction. In Figure 4.6 the full model picturing the emerging crack at the maximum indentation depth is shown. The crack opening in the x-direction is scaled by a factor of 10. During the unloading the crack continues to grow slightly downwards.

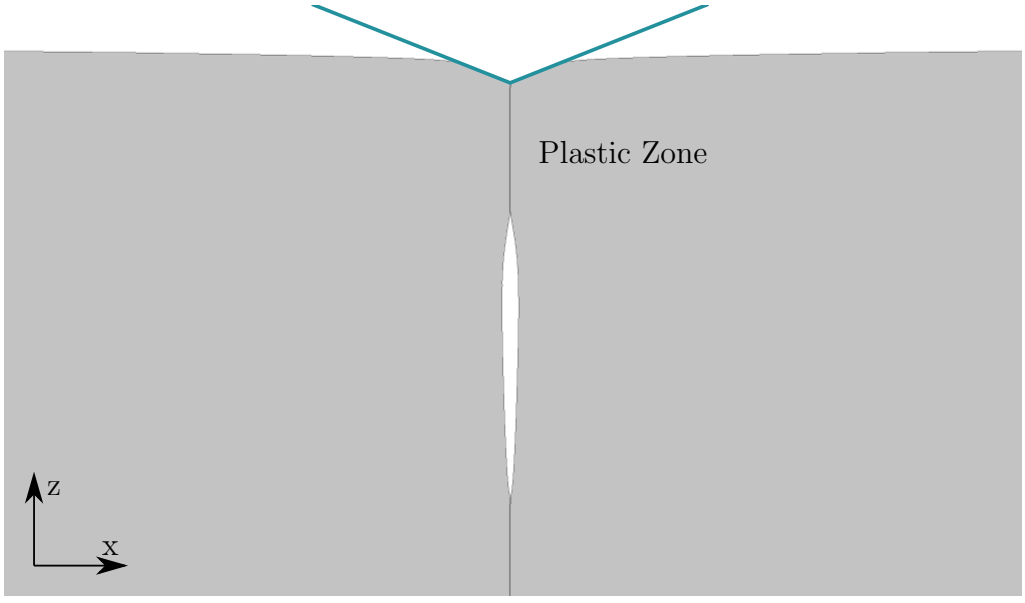


**Figure 4.6:** Formed crack during the 2D simulation at an indentation depth of 0.365 µm. The crack opening in the x-direction is scaled by a factor of 10. The crack has a length of 2.685 µm.

## 4.2 3D Nanoindentation Model

In this section the outcomes of the three-dimensional model are presented and discussed. Since information from various experiments is available, simulations with indentation depths from 0.25 µm to 1.0 µm are conducted. The results are then compared to the experimental data from the KAI, Villach.

Due to the high increase in the number of degrees of freedom in the 3D model, small element edge lengths as in the 2D simulations are no longer efficient. In order to be able to use an element edge length of about 0.1 µm, a reduction of the fracture strength is necessary. Furthermore a similar stress state as described in Section 4.1.2 is observed. Therefore, the fracture strength reduction is necessary in order to simulate the crack emergence and propagation. Unless otherwise stated, a fracture strength of 1 GPa is used in the following simulations.

### 4.2.1 Structural Response

#### Load-Penetration Curve

Figure 4.7 shows the load-penetration curve predicted by the simulation compared to the experimental results for an indentation depth of 0.365 µm. The FEM simulation corresponds very well to the data obtained in the experiments. Since the crack formation and propagation has a negligible effect on the load-penetration diagram, the curves coincide with the plots in [11]. The maximum load is 0.035 76 N in the FEM model and on average 0.035 85 N in the experiments. The load controlled experimentally obtained curves show a time dependant behaviour during the dwell time at the highest indentation force. This response cannot be modelled, since no time dependency is considered. Due to the deviation of the loading and unloading curves, energy dissipation owing to plastic deformation is indicated. A residual imprint with a depth of 0.219 µm remains after the indentation, according to the FEM computation.

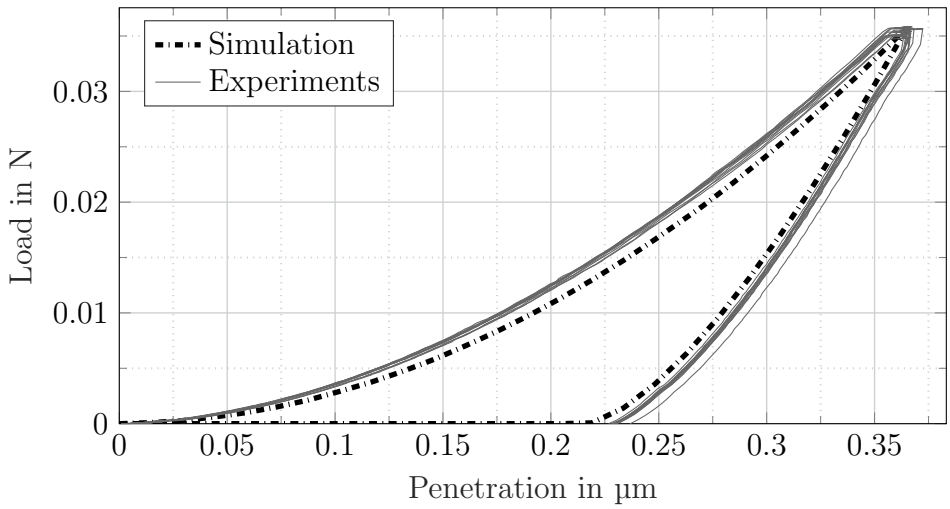


**Figure 4.7:** Predicted load-penetration curve for an indentation depth of 0.365 µm. Results obtained from simulations and experiments are compared.

In Figure 4.8 the load-penetration curve predicted by the simulation is compared to the experimental results for an indentation depth of 1.0 µm. The diagram shows a deviation from the experimental results. The maximum load is 0.2699 N in the FEM model and on average 0.2328 N in the experiments. After the indentation process a residual indent of 0.6114 µm is predicted in the simulations, whereas 0.6201 µm are measured on an average during the experiments. There is a strong similarity between the outcomes of the experiments and the results of the simulations.

Because of the high indentation depth, the impact of the silicon substrate becomes more essential. The predicted behaviour in the simulation is found to be stiffer than expected. The discrepancy of the unloading curve indicates an inaccurate elastic response of the materials. The simplification concerning the elastic behaviour of $\langle 111 \rangle$ Si are a possible cause of the diverging results. Since the elastic material parameters of the actually tested structure are not known, various values for GaN and Si found in the literature are compared in [11]. It is presumable that the parameters leading to a strong consistency with experimental results for low indentation depths do not display the behaviour of the structure under high indentation loads. Furthermore the

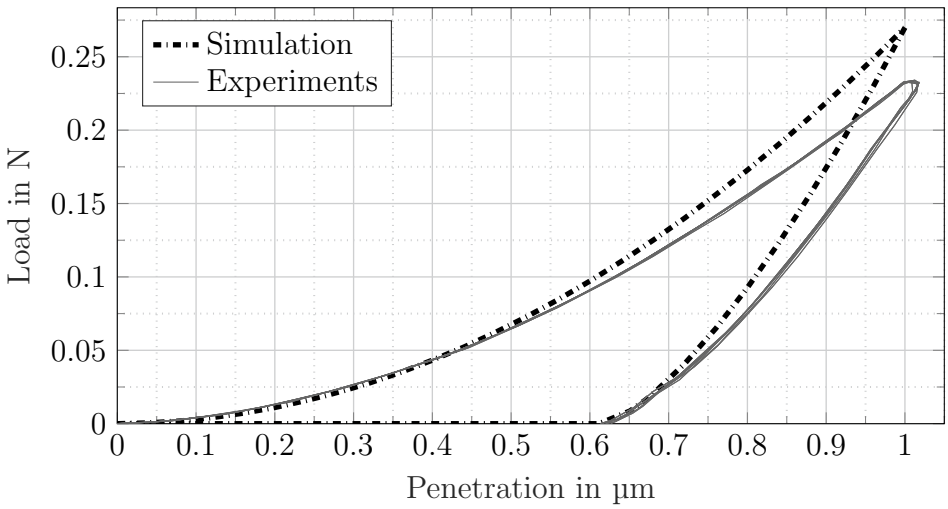


**Figure 4.8:** Predicted load-penetration curve for an indentation depth of 1.0 µm. Results obtained from simulations and experiments are compared.

parameters describing the plastic behaviour of GaN in [11] might be inaccurate for higher indentation depths.

### Energy Considerations

Figure 4.9 and Figure 4.10 show the energy distribution over the step time of the simulation. The diagrams correspond to an indentation depth of 0.365 µm. The structural behaviour is comparable to the 2D simulations. There is a large amount of dissipated energy due to plastic deformation, increasing immediately upon loading. The fracturing of the wafer leads to a significantly smaller amount of energy dissipation compared to plasticity. The plastic deformation leads to a dissipation of $2.11626 \cdot 10^{-3}$ Nµm, the crack emergence and propagation to $9.93227 \cdot 10^{-6}$ Nµm. Hence, it is obvious that fracture has no influence on the load-penetration curve in the nanoindentation simulations.

After the indentation process residual stresses are introduced into the material.

The elastic energy in the interface elements is comparatively small to all other energies in the system. Therefore it is not indicated in the resulting line plots.

During the simulation only a small amount of viscous damping is needed. The dis-

sipated energy due to the viscous regularization is 2.8432 % of the dissipation owing to fracture.

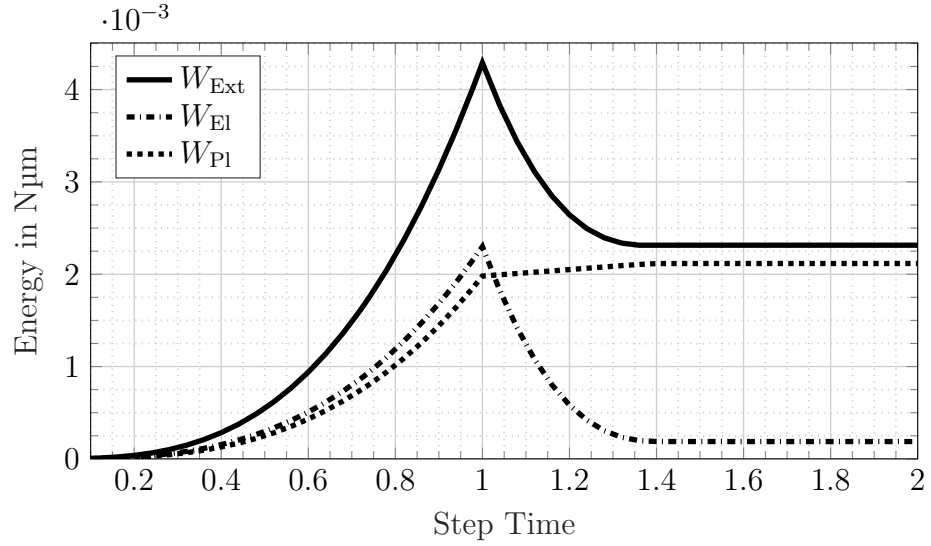


**Figure 4.9:** Applied external energy $W_{\mathrm{Ext}}$, elastic strain energy $W_{\mathrm{El}}$ and plastic dissipated energy $W_{\mathrm{Pl}}$ during the indentation. Step time 0-1 corresponds to the penetration, 1-2 to the unloading of the structure.

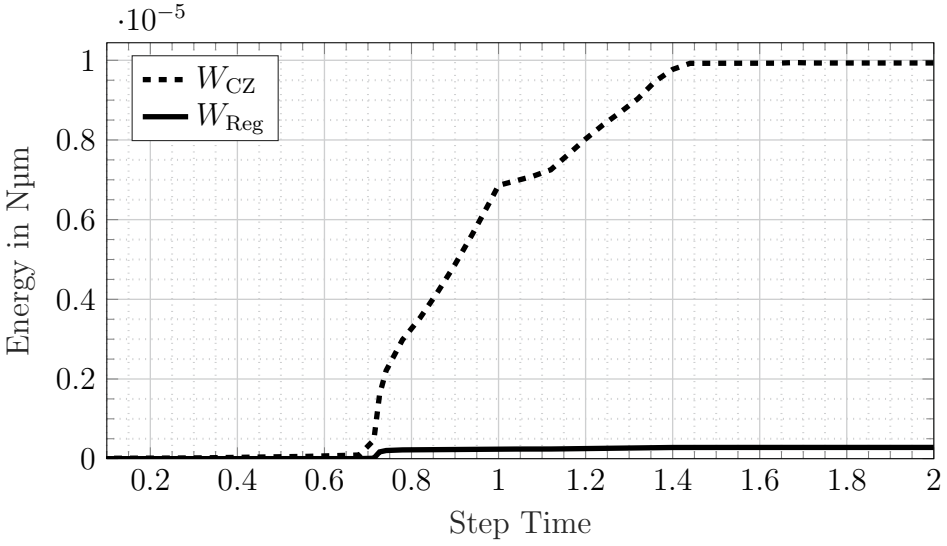


**Figure 4.10:** Dissipated energy due to fracture $W_{\mathrm{CZ}}$ and viscous regularization $W_{\mathrm{Reg}}$. Step time 0-1 corresponds to the penetration, 1-2 to the unloading of the structure.

### Residual Imprint and Cracks

This section considers the residual imprint and the cracks, visible at the GaN surface. The wafer has been analysed using NanoVision scans and furthermore an optical microscope after the experimental testing by the KAI, Villach. Using the NanoVision, the nanoindenter tip can be used to scan the surface of the wafer similar to an atomic force microscope after an indentation. The accuracy depends on the condition of the diamond tip and the precision of the used measuring equipment [1].

Figure 4.11 shows the residual imprint measured with the NanoVision (a) and the displacements in the z-direction of a simulation (b) in µm. Both imprints result from an indentation of 1.0 µm. Since the resolution of the NanoVision is not accurate enough to display the occurring cracks, they are suppressed in the FEM plot. The size and the shape of the imprint is very similar. The maximum residual indentation depth is 0.536 µm in the measurements, 0.6114 µm in the FEM simulations. This non-conformance is most likely caused by the limitations of the NanoVison measurements.

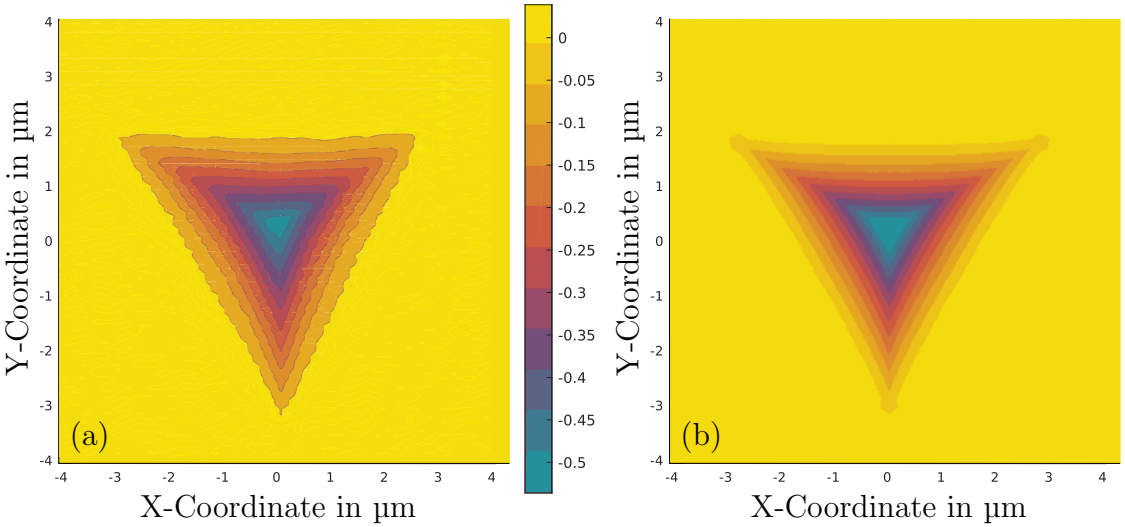


**Figure 4.11:** Depth of the residual imprint measured with the NanoVision technology (a) and FEM results (b) in µm.

In the experimental load-penetration curve in Figure 4.8 a residual indentation depth of 0.6201 µm is observable, as described earlier in this section.

The surface cracks are evaluated using an optical microscope by the KAI, Villach. In Figure 4.12 a microscope image of a residual imprint with radial cracks emerging from the indenter edges is shown. The averaged measured crack length from the centre of the indentation to the crack edge is 6.92 µm, although the resolution of the image only allows a rudimentary length evaluation. Figure 4.13 depicts the resulting crack on the wafer surface, as predicted in the FEM simulation. The FEM model leads to a crack length of 9.23 µm. Both in the experiments and in the simulations an indentation depth of 1.0 µm is used. The crack length obtained in the simulations exceeds the measured size. The influence of the material parameters on the crack length is considered in Section 4.2.3.

The results of the FEM simulations give the possibility to evaluate the cracks not only at the surface but also of the sub-surface crack size and shape. In the next section crack emergence and propagation are studied in detail.

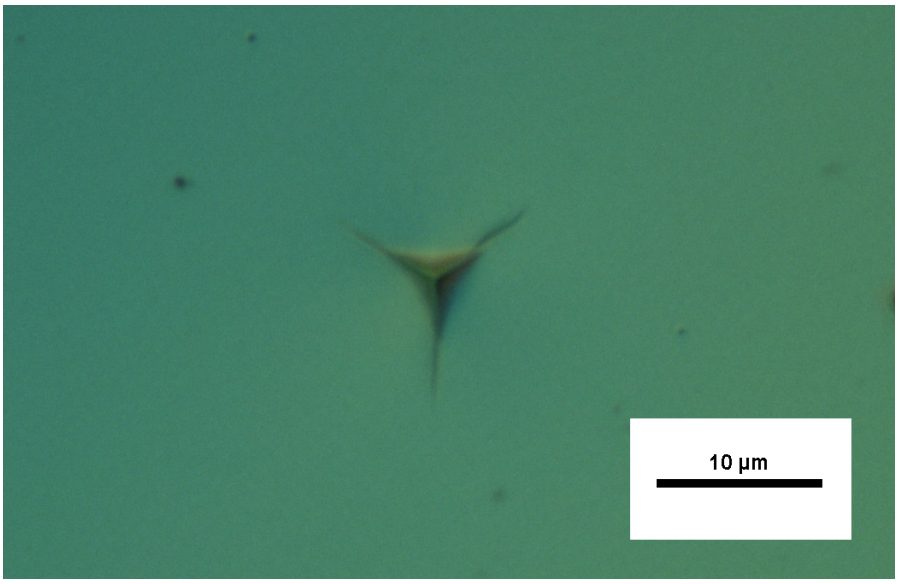


**Figure 4.12:** Optical microscope image of a residual impression and cracks in GaN after nanoindentation with an indentation depth of 1.0 µm.

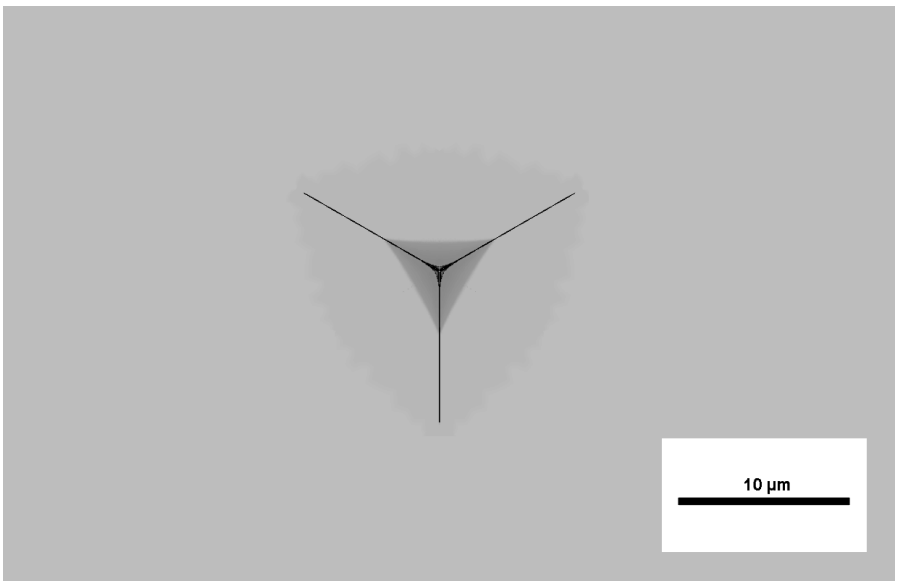


**Figure 4.13:** Residual impression and cracks in GaN after nanoindentation with an indentation depth of 1.0 µm, predicted by the FEM simulation.

### 4.2.2 Crack Emergence and Propagation

The emerging cracks are computed for indentation depths of 0.25 µm up to 1.0 µm. First of all, a simulation without interface elements is run, evaluating the tensile stresses perpendicular to the crack faces throughout the indentation process. A maximum tensile stresses of $\sigma_{yy} = 1.273\,\text{GPa}$ occurs below the compressive, plastically deformed zone during the penetration of the wafer. The used fracture strength needs to be smaller than this value, in order to simulate crack emergence.

Figure 4.14(a) shows the denotion of the two crack planes. Crack plane 1 is aligned with the indenter edge. Crack plane 2 corresponds to the second symmetry plane. In Figure (b) the part of the crack plane presented in the following figures in this chapter is depicted. The images show GaN top layers on a Si substrate as outlined in Figure 4.14(c). In the crack figures in the following sections, blue corresponds to undamaged material, green to partially damaged regions and red to failed areas. Therefore, the red sections indicate a crack.

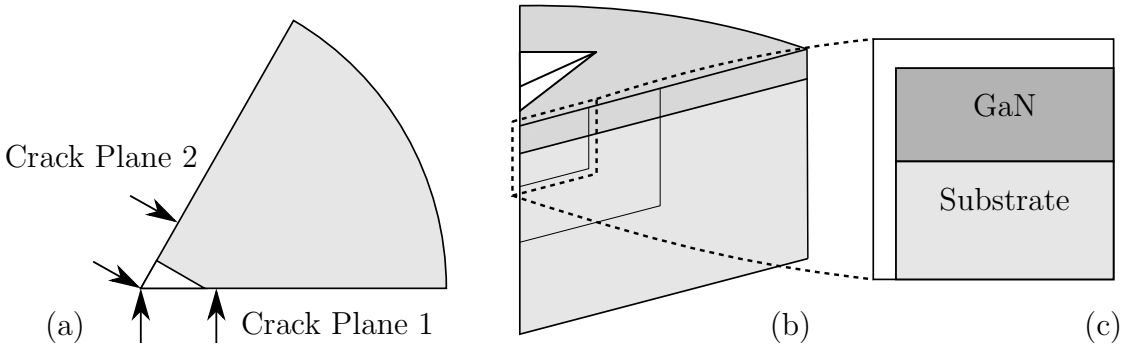


**Figure 4.14:** (a) Denotation of the two crack planes. (b) Part of the crack plane depicted in the following figures. (c) GaN layers are shown on top of the Si substrate.

The process of crack emergence and propagation is explained using a simulation with an indentation depth of 0.365 µm. A time sequence of the crack growth on crack plane 1 is shown in Figure 4.15. The fine meshed region is pictured. The figures correspond to the points in the schematic load-penetration curve on the top right. Figure 4.15(a) shows the crack at an indentation depth of 0.292 µm. The crack emerges under the plastically deformed, compressive zone and grows radially outwards. In Figure 4.15(b) the crack is shown at the maximum indentation depth. Since Si exhibits a higher critical energy release rate, more energy is needed in order to extend a crack. Therefore a discontinuity of the crack is visible, leading to a smaller crack in the substrate. Figure 4.15(c) presents the crack during the unloading at an indentation depth of 0.305 µm. The crack increases further in radial direction and grows upwards. Next do the indenter edge a small Palmqvist crack emerges. Throughout further unloading this crack merges with the sub surface crack and enlarges in radial direction on the wafer surface. In Figure 4.15(d) the crack shape at the end of the indentation process is shown. In the plastically highly deformed region no crack emerges.

Below the indenter a small crack emerges very early during the penetration. This is caused by the excessive stresses due to the concentration directly below the sharp indenter tip.

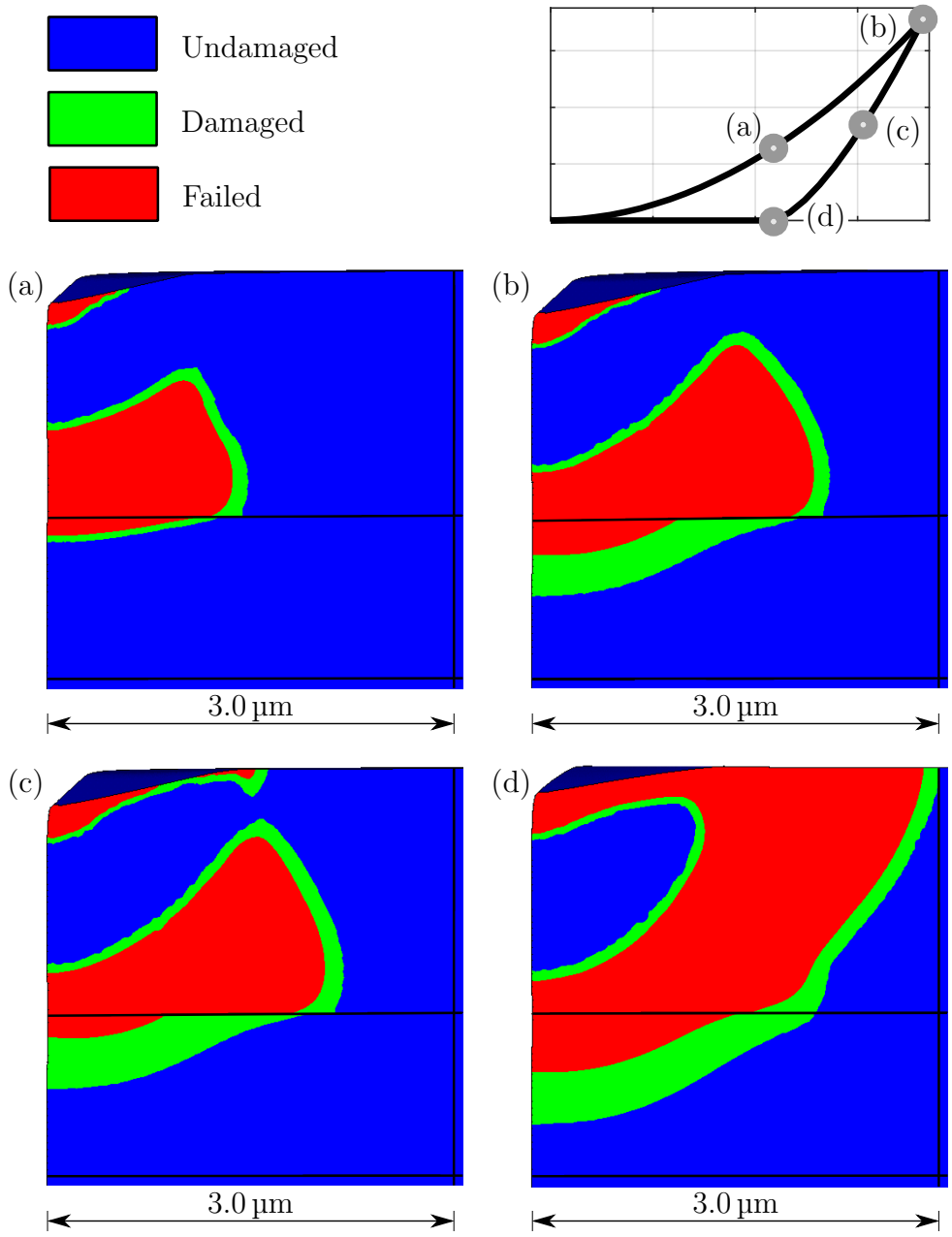


**Figure 4.15:** Cracks in crack plane 1 during the indentation at (a) 0.292 µm, (b) 0.365 µm and during unloading at (c) 0.305 µm. (d) Final crack shape. The points in the schematic load-penetration curve on the top right correspond to the figures.

The shape of the crack is different to the ones observed in [28]. Instead of median cracks, a quarter-penny crack is formed. This difference is based on the resulting stress state, owing to the elasto-plastic material definition. While unloading, the elastic strain field decreases, whereas the arising residual stresses around the plastic zone lead to a further opening of the crack.
The surface crack at the end of the simulation shows a length of 2.985 µm.

In Figure 4.16 crack plane 2 after the indentation with a depth of 0.365 µm is shown. Only a minor crack emerges in the GaN layer during the penetration, since the crack driving forces perpendicular to the crack plane are way smaller compared to crack plane 1. A small region under the interface is partially damaged. While the unloading of the wafer the crack does not enlarge.
Using higher indentation depths, no noteworthy cracks emerge in this plane. Merely the partially damaged region in the Si substrate extends further downwards from the interface. The energy dissipation due to crack emergence in crack plane 2 is therefore negligible.

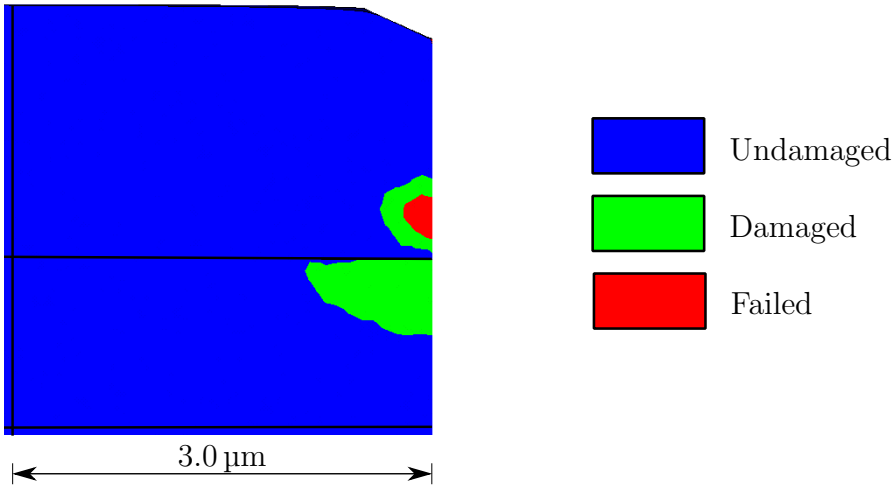


**Figure 4.16:** Crack plane 2 after the indentation with a depth of 0.365 µm. Only a small crack emerges in the GaN layer.

Higher indentation depths lead to an increase in the crack size in crack plane 1, as shown in Figure 4.17. A crack emerging due to an indentation with a depth of 1.0 µm is depicted. The occurring crack reaches far down into the Si substrate. Even during loading the crack almost reaches the surface of the wafer. The surface crack at the end of the simulation shows a length of 9.23 µm.

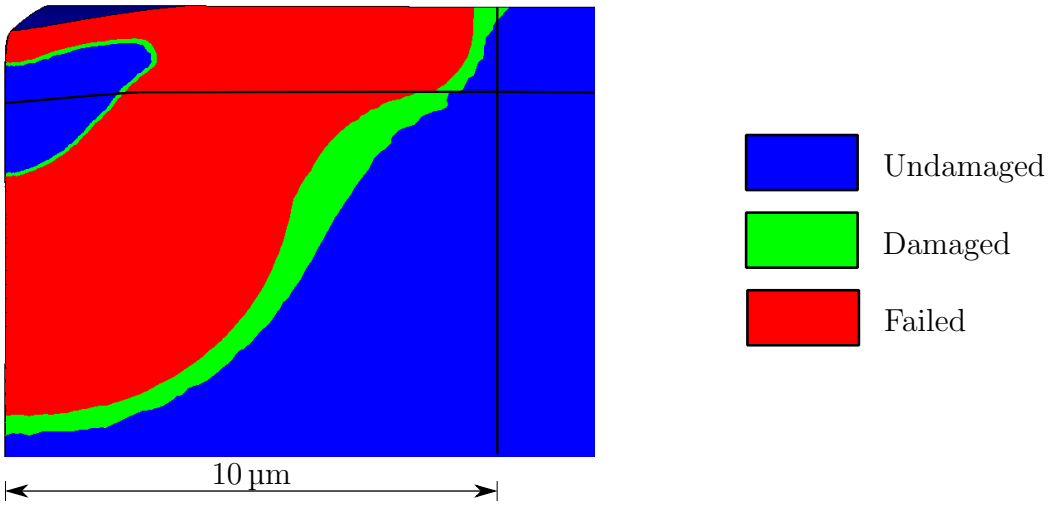


**Figure 4.17:** Crack plane 1 after the indentation with a depth of 1.0 µm.

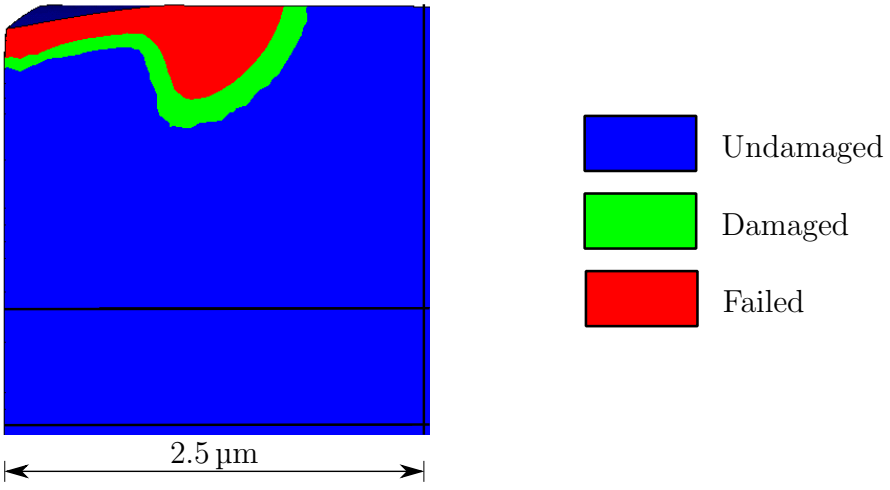


**Figure 4.18:** Crack plane 1 after the indentation with a depth of 0.25 µm. A Palmqvist crack emerges next to the indenter edge during unloading.

If the indentation depth is too small, so that the tensile stresses under the plastically deformed area do not reach the fracture strength, no crack emerges during the penetration. A crack forming during the unloading step of an indentation to a depth of 0.25 µm is shown in Figure 4.18. A Palmqvist crack emerges next to the indenter edge.

In Figure 4.19(a) the dissipated energy due to fracture is shown over the step time for various indentations. Five simulations using penetration depths from 0.365 µm to 1.0 µm are conducted. The dissipation increases with higher indentation depths, both during loading and unloading. The dissipation caused by fracture of the material increases approximately quadratically with the indentation depth in the regarded interval, as visible in Figure 4.19(b). In this diagram the dissipated energy after the indentation process is shown over the penetration depth. Since the critical energy release rate is constant in these simulations, the crack area is direct proportional to the dissipated energy in the interface, and therefore increases quadratically as well.

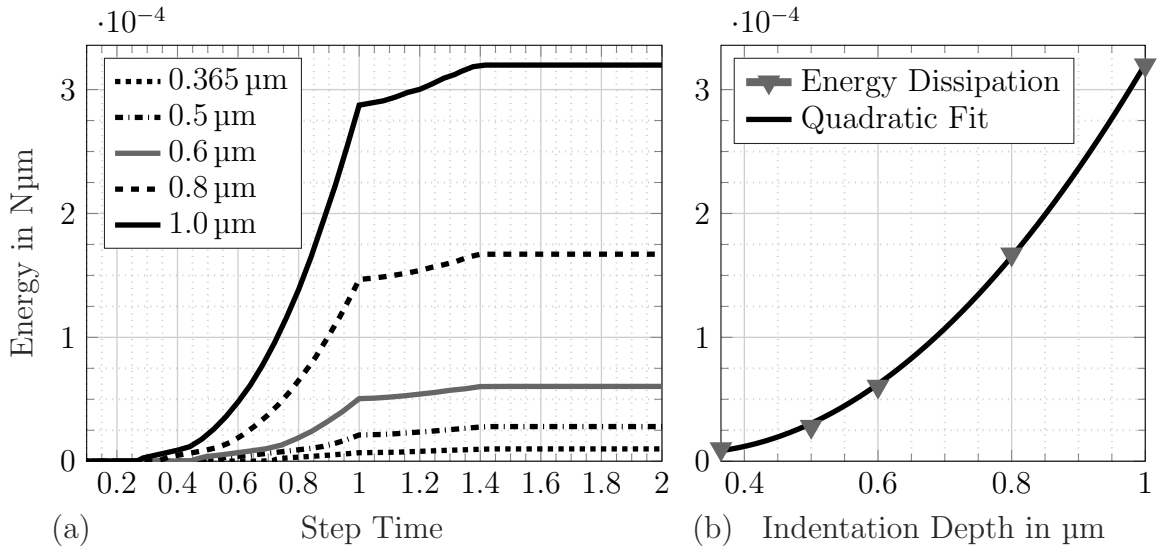


**Figure 4.19:** (a) Dissipated energy caused by fracture over the step time for various indentation depths. Step time 0-1 corresponds to the penetration, 1-2 to the unloading of the structure. (b) Quadratic increase of dissipated energy in the CZ over the indentation depth.

Figure 4.20 shows a comparison of the surface crack length resulting from simulations and experiments for indentations with various depths. The average crack length is measured using optical microscope images prepared by the KAI, Villach. The crack lengths predicted by the numerical model is evaluated at the end of the simulation. As shown in diagram 4.19(b) the crack area increases quadratically with the indentation depth, whereas the surface crack increases linearly. Between 0.6 µm and 0.8 µm the gradient increases. This phenomenon occurs in the simulations as well as in the experimental results. The measured results and the predicted cracks in the simulation show very similar slopes, however, numerical results exceed the experimental findings. The simulation model leads to longer cracks than the ones obtained in the measurements.

All these simulations indicate the emergence of half-penny cracks after the indentation process.

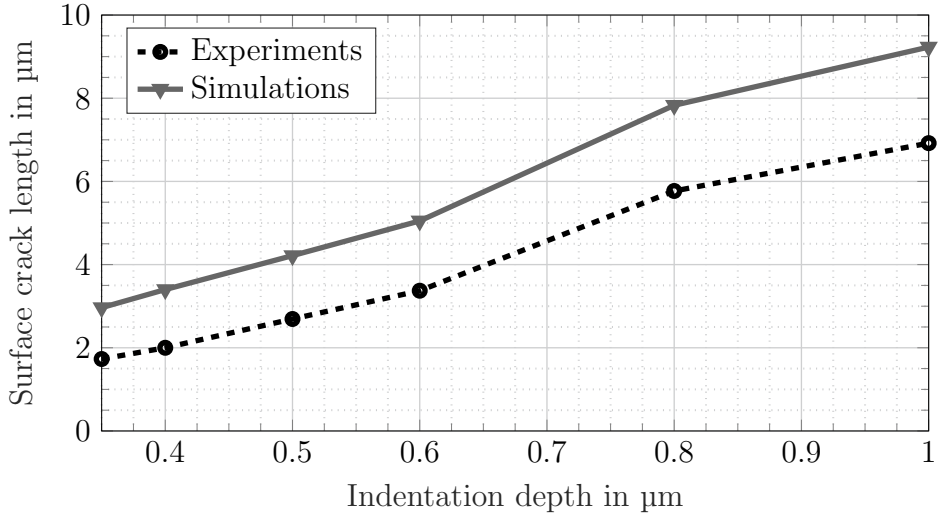


**Figure 4.20:** Comparison of the resulting surface crack length from the FEM simulations and nanoindentation experiments by the KAI, Villach.

### 4.2.3 Influence of Fracture Strength and Fracture Toughness

The fracture strength should not have an influence on the energy dissipation in the simulations. Various fracture strength parameters are studied and compared in Figure 4.21. The smallest value used is 0.5 GPa, the maximum 1.25 GPa, which is close to the highest tensile stress perpendicular to the crack plane. An indentation depth of 0.365 µm is simulated. The energy that is dissipated due to fracture during the entire indentation process is nearly constant. The change of the fracture strength leads to a variation of the energy of only about 2.44 %. Moreover, the final crack size and shape are not affected either. Even a high fracture strength value of 1.25 GPa does not affect the crack propagation. However, the step time where fracture begins to occur changes with the fracture strength. A higher interface strength leads to a postponed crack emergence. Once the crack is formed, the crack size and shape is influenced by the potential energy that is available to extend a the crack front.
The load-penetration curve or other results are not influenced by the choice of fracture strength.

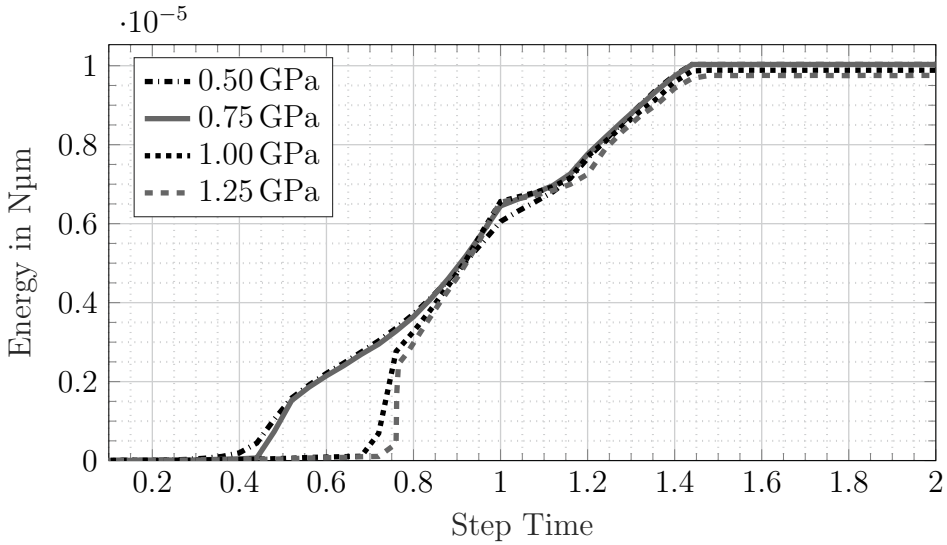


**Figure 4.21:** Comparison of the dissipated energy due to fracture for different fracture strengths. Step time 0-1 corresponds to the penetration, 1-2 to the unloading of the structure.

Figure 4.22 shows the influence of the critical energy release rate on the crack in the simulations. Simulations are run with the initial value and with increased parameters up to the quadruple value. An indentation depth of 0.365 µm is simulated. A higher critical energy release rate leads to less dissipation and therefore a small crack, since more energy is needed to extend a crack. The crack emergence step time is only slightly influenced by the critical energy release value.

In the literature higher fracture toughness values are stated for GaN, compared to the used parameters in the simulations [34]. A higher fracture toughness, and therefore increased critical energy release rate, results in smaller cracks in the FEM simulations. A fracture toughness $1.55\,\mathrm{MPa}\sqrt{\mathrm{m}}$ leads to a critical energy release rate of $8.0662\,\mathrm{N\,m^{-1}}$, which is 15 times the initially used value. Using this parameter in the simulations no crack arises at an indentation depth of 0.365 µm, and only a small crack but large partially damaged area at 1.0 µm. Compared to the experimental results, using this high fracture toughness leads to an underestimation of the crack lengths.

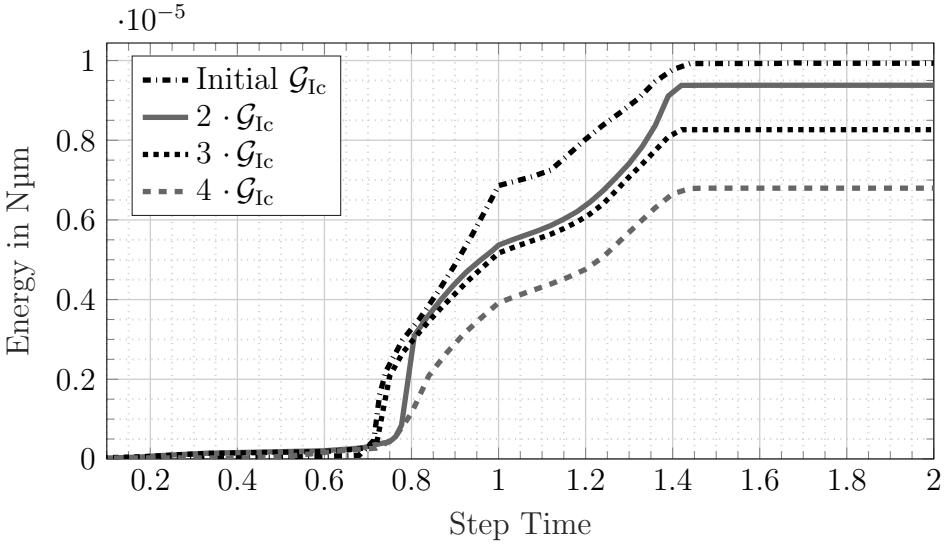


**Figure 4.22:** Comparison of the dissipated energy in the cohesive zone for different critical energy release rates. Step time 0-1 corresponds to the penetration, 1-2 to the unloading of the structure.

### 4.2.4 Influence of Residual Stresses

In this section the emerging cracks in stacked layered wafers including residual stresses are studied. The considered stack designs are described in Figure 3.6. In all the following simulations an indentation depth of 0.365 µm is used.
A special assessment concerning the fracture strength has to be made. If the residual stresses in a layer exceed the fracture strength, the cohesive elements are damaged even before the indentation. In order to prevent this, the fracture strength needs to be increased well above this stress level. In the simulations a fracture strength of 1 GPa higher than the maximum tensile stress in the layered structure is used.
Due to the residual stresses, an additional elastic strain energy is introduced into the model.

Figure 4.23 shows the elastic strain energy and the dissipation due to plastic deformation over the step time simulating a stack sequence including residual stresses. It is apparent that a specific amount of elastic energy is present before the inden-

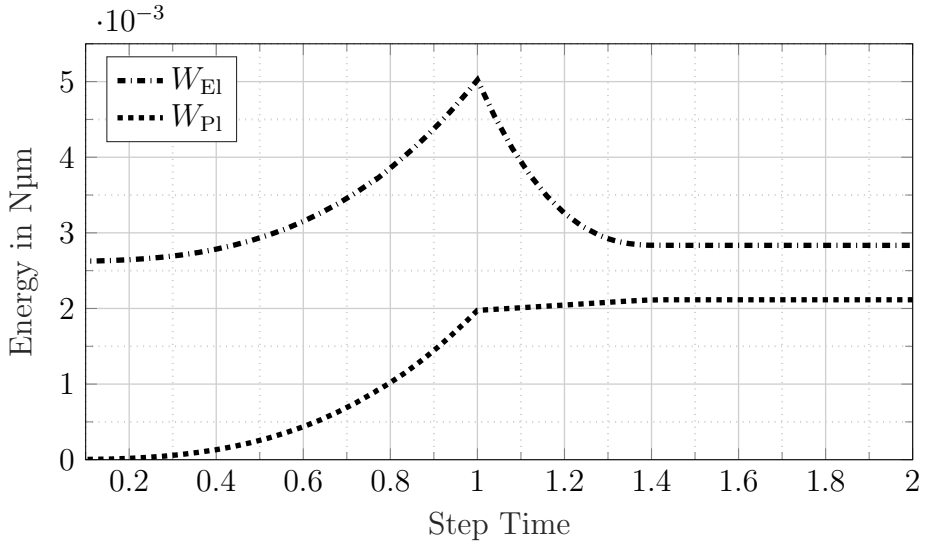


**Figure 4.23:** Elastic $W_{\mathrm{El}}$ and plastic $W_{\mathrm{Pl}}$ strain energy. Since residual stresses are present, there is an initial amount of elastic strain energy. Step time 0-1 corresponds to the penetration, 1-2 to the unloading of the structure.

tation. The increase during the loading and the decrease while unloading, however, is comparable to simulations without residual stresses. This energy is introduced in the model due to the indentation. Since the biaxial stresses are incorporated in the whole layers, the additional elastic strain energy is dependent on the model size. If a bigger model size is used, this energy increases. Due to the enlarged amount of potential energy, more energy is available to grow a crack, which leads to bigger crack sizes. Simulations using different model sizes are run, in order to study the influence of the geometry on the crack behaviour. The crack only emerges in a small part of the model. Therefore, it is found that the model size does not affect the fracture behaviour in the simulations. A radial length of 25 µm is found to be sufficient.

Due to the residual stresses, the interface elements are initially stressed. Due to the magnified fracture strength the elements are not damaged. The residual stresses have a negligible influence on the plastic behaviour as well as the predicted load-penetration curve. This findings agree with the results in [11].

Simulations including residual stresses are found to be more complex in terms of convergence behaviour and hence, computation times. Due to bigger cracks, the fine meshed regions need to be enlarged. This leads to an additional increase in calculation times.
More energy dissipation by the viscous regularization is used in order to achieve numerical convergence. Approximately 7 % to 15 % of the energy in the cohesive zone elements is dissipated due to the viscous damping.
In crack plane 2 no sizeable cracks arise during the simulations in this section.

**Uniform Stress in GaN Layer**

A simulation is run with a residual stress state shown in Figure 3.6(a). The dissipated energy due to fracture over the step time is shown in Figure 4.24.

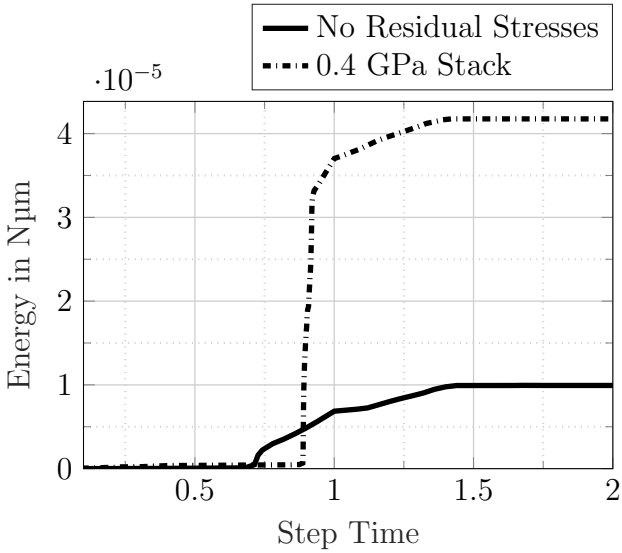


**Figure 4.24:** Comparison of the dissipated energy due to fracture of the considered stack and the initially unstressed structure. Step time 0-1 corresponds to the penetration, 1-2 to the unloading of the structure.

The result is compared to the outcome of the simulations without residual stresses. The dissipated energy during this simulation exceeds the compared model by far. At a step time of about 0.8 unstable crack growth occurs for a short period. Since a rather big crack emerges, the cracked area exceeds the fine meshed region. A further refinement of the mesh would lead to an excessive increase in calculation time and is therefore omitted. In this simulation the highest amount viscous regularization of about 15 % of the energy dissipated in the cohesive zone elements is needed.

### Stack considered in [29]

A simulation is run with a residual stress state shown in Figure 3.6(b). Since the stress distribution is measured in [29], this stack represents a rather realistic wafer, compared to the stack described above. The dissipated energy due to fracture over the step time is shown in Figure 4.25. The result is compared to the outcome of the simulations without residual stresses.

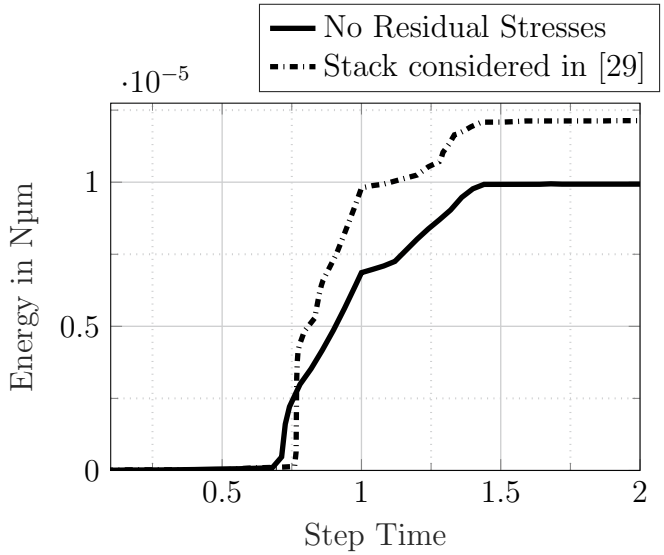


**Figure 4.25:** Comparison of the dissipated energy due to fracture of the stack considered in [29] and the initially unstressed structure. Step time 0-1 corresponds to the penetration, 1-2 to the unloading of the structure.

The two simulations show comparable results. Since tensile and compressive stresses are present in the layered stack, unstable crack growth is prevented for the most part. Unstable growth takes place only briefly after the crack emergence.

In Figure 4.26 the resulting crack after the indentation is shown. The size and shape of the crack is similar to the one with no initial stressed layers. In the figure the individual layers are apparent. The top layer and the Si substrate on the bottom of the stack exhibit no residual stresses. Regarding the surface crack, nearly no difference is found compared to the initially unstressed structure. Since the residual stress state is mostly unknown, they can be a source of error, if the surface cracks are used to obtain material parameters. In the presence of residual stresses the surface crack length cannot be used to draw conclusion of the dissipated energy.

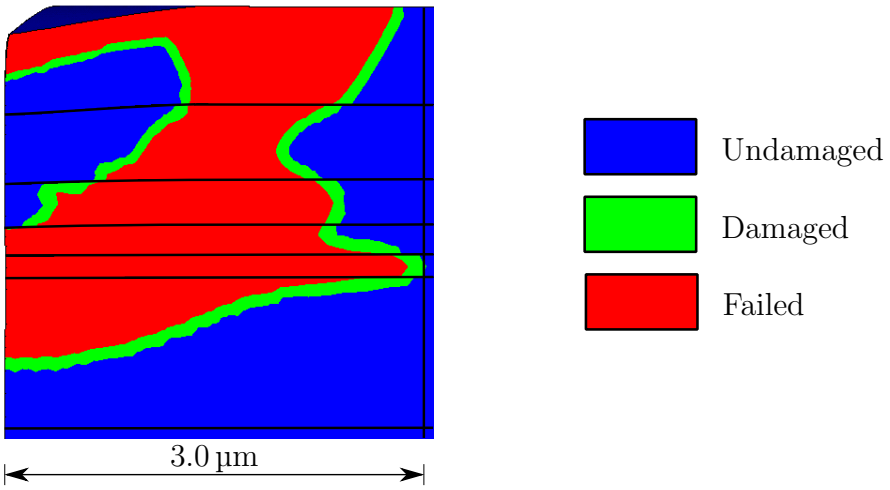


**Figure 4.26:** Crack plane 1 after the indentation with a depth of 0.365 µm in the stack considered in [29].

### Test Stack 1 and 2

Simulation are run with residual stress states as shown in Figures 3.6(c) and (d). The dissipated energy due to fracture over the step time is shown in Figure 4.27. The results are compared to the outcome of the simulations without a residual stress state. In both simulations temporarily unstable crack growth takes place.

Figure 4.28 presents the resulting cracks after the indentation process. The layers of the stacked structure are visible. Figure 4.28(a) shows the cracks in Test Stack 1. The crack starts to emerge under the plastically deformed zone but is prohibited to grow upwards due to the compressive stress layer. During the unloading a Palmqvist crack emerges at the surface. It is visible that the crack grows into an area with larger element sizes.

In Figure 4.28(b) the final crack in Test Stack 2 is shown. Since the compressive layer is placed directly above the GaN-Si interface, the crack is prevented from growing into the Si substrate. However, the tensile stresses near the top of the wafer lead to a big surface crack.

The energy dissipated in Test Stack 1 exceeds Test Stack 2 although the surface crack in the second stack is much larger. Again, measuring the surface crack length would give misleading results.

Tensile stressed layers lead to temporarily unstable crack growth, whereas compressive layers tend to prevent further crack extension.

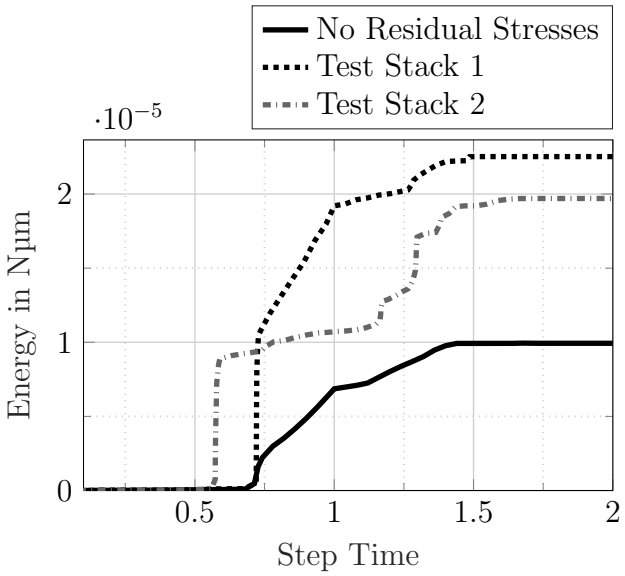


**Figure 4.27:** Comparison of the dissipated energy due to fracture of the considered stacks and the initially stress free structure. Step time 0-1 corresponds to the penetration, 1-2 to the unloading of the structure.

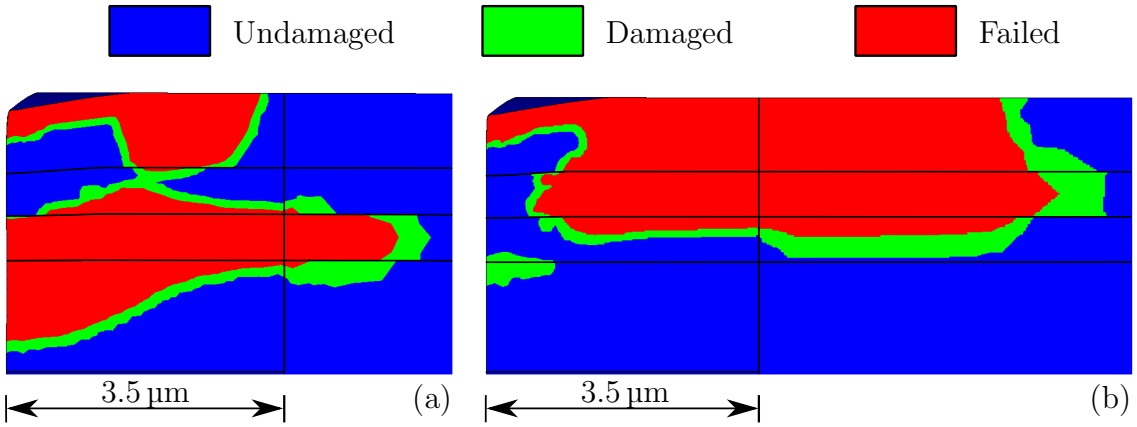


**Figure 4.28:** Crack plane 1 after the indentation with a depth of 0.365 µm in (a) Test Stack 1 and (b) Test Stack 2.

# Chapter 5

# Summary

In this final chapter, a short summary of the presented methods and results is given and the major findings are highlighted. Moreover, further interesting aspects that exceed the scope of this thesis are presented in a short outlook.

In this thesis a numerical, non-linear nanoindentation Finite Element Model, that is able to predict the energy dissipation due to plastic deformations and furthermore, the crack emergence and propagation is established. The instrumented indentation testing in Gallium Nitride on a Silicon substrate using a Berkovich indenter tip is simulated.
To model the anisotropic plasticity Hill's potential is utilised, approximating the single crystal plasticity of GaN. The fracture process is simulated using cohesive interface elements placed in the potential crack planes. To keep the numerical effort and therefore computation times rather low, a symmetry model is used. The influence of various material parameters, such a fracture strength and fracture toughness is investigated. The available experimental data from the KAI GmbH, Villach is used to be compared to the numerical results. Furthermore, the influence of residual stresses in the top layers of the wafer on fracture behaviour is studied.

The predicted load-penetration curves show similar results than the obtained experimental data. The optical inspection of the wafer surface after the indentation process reveals similar residual imprints and surface cracks than the FEM simulations. The numerical model tends to show longer cracks than observed in the experiments. The simulations indicated that the dissipated energy due to plastic deformations is much higher than the energy used for crack emergence and propagation. Hence, the energy dissipated as a result of fracture is not apparent in a load-penetration curve. The simulations show crack growth during the penetration and furthermore while unloading of the wafer, leading to a quarter-penny crack. Small indentation depth lead to a Palmqvist crack emerging next to the indenter edges. Since the crack emergence occurs at intersecting slip planes or due to pre-existing flaws in the material, a reduction of the fracture strength is needed in order to simulate the fracturing process. The selection of fracture strength has no influence on the crack size and shape. It is found that residual stresses in the layered stack have a high influence on fracture behaviour. The additional potential elastic energy induces further crack growth. Tensile stresses lead to temporarily unstable crack growth, resulting in large cracks, whereas compressive stresses have positive influence, mitigating the crack extension. The numerical model in combination with the applied approaches gives useful capabilities for computational investigations of cracks, emerging during nanoindentation experiments. A variety of residual stress states can be studied in a rather short time and their effect on the fracture behaviour of semiconductor materials predicted.

### Outlook

In this thesis the primarily radial cracks and the influence of plasticity on the crack emergence and propagation is studied.
The FEM model could be developed further by including potential lateral cracks and the delamination of individual layers, as observed in some experiments. Thereby the lateral crack behaviour can be studied and possible interactions of the cracks considered.
Since different residual stress distributions occur in the layers on the outside of a wafer, free edge effects have a potential influence on the fracture behaviour and delamination.
Another interesting aspect is the direction dependent development of the plastic strains under the indention loads. It is of interest if the Hill's plasticity model has the capabilities to predict plastic deformations in single crystal materials.

# Bibliography

[1] Agilent Technologies, Inc., 1601 California Street Palo Alto, CA 94304 USA. *NanoVision - User's Guide*, August 2010.

[2] T. L. Anderson. *Fracture Mechanics: Fundamentals and Applications*. CRC Press, 2005.

[3] ANSYS Inc., Canonsburg, PA, USA. *ANSYS Academic Research Mechanical, Release 18.2, Mechanical APDL Documentation*, 2017.

[4] G. E. Dieter. *Mechanical metallurgy*. McGraw-Hill series in materials science and engineering. McGraw-Hill, 1986.

[5] A. C. Fischer-Cripps. *Nanoindentation*. Springer-Verlag New York, 2011.

[6] Y. F. Gao and A. F. Bower. A simple technique for avoiding convergence problems in finite element simulations of crack nucleation and growth on cohesive interfaces. *Modelling and Simulation in Materials Science and Engineering*, 12(3):453, 2004.

[7] D. Gross and T. Seelig. *Fracture Mechanics - With an Introduction to Micromechanics*. Springer International Publishing, 2018.

[8] J. T. Hagan and M. V. Swain. The origin of median and lateral cracks around plastic indents in brittle materials. *Journal of Physics D: Applied Physics*, 11(15):2091, 1978.

[9] J. Hay. Introduction to instrumented indentation testing. *Experimental Techniques*, 33(6):66 – 72, 2009.

[10] R. Hill. *The Mathematical Theory of Plasticity*. Oxford engineering science series. Clarendon Press, 1983.

[11] P. Hoffmann. Elasto-plastic finite element simulations of nanoindentation problems utilizing Hill's potential. Master's thesis, ILSB, TU Vienna, 2018.

[12] M. A. Hopcroft, W. D. Nix, and T. W. Kenny. What is the young's modulus of silicon? *Journal of Microelectromechanical Systems*, 19:229–238, 2010.

[13] H. C. Hyun, F. Rickhey, J. H. Lee, J. H. Hahn, and H. Lee. Characteristics of indentation cracking using cohesive zone finite element techniques for pyramidal indenters. *International Journal of Solids and Structures*, 51(25):4327 – 4335, 2014.

[14] S.-R. Jian. Berkovich indentation-induced deformation behaviors of GaN thin films observed using cathodoluminescence and cross-sectional transmission electron microscopy. *Applied Surface Science*, 254(21):6749 – 6753, 2008.

[15] K. E. Johanns, J. H. Lee, Y. F. Gao, and G. M. Pharr. An evaluation of the advantages and limitations in simulating indentation cracking with cohesive zone finite elements. *Modelling and Simulation in Materials Science and Engineering*, 22(1):015011, 2014.

[16] J. Kim, D. I. D. Cho, and R. S. Muller. Why is (111) silicon a better mechanical material for MEMS? pages 662–665, 2001.

[17] C. Kittel. *Introduction to Solid State Physics*. Wiley, 2004.

[18] M. Kuna. *Finite Elements in Fracture Mechanics - Theory - Numerics - Applications*. Springer Netherlands, 2013.

[19] B. R. Lawn, A. G. Evans, and D. B. Marshall. Elastic/plastic indentation damage in ceramics: The median/radial crack system. *Journal of the American Ceramic Society*, 63(9 - 10):574 – 581, 1980.

[20] J. Lee, Y. Gao, K. Johanns, and G. Pharr. Cohesive interface simulations of indentation cracking as a fracture toughness measurement method for brittle materials. *Acta Materialia*, 60(15):5448 – 5467, 2012.

[21] F. Medjdoub. *Gallium Nitride (GaN): Physics, Devices, and Technology*. Chapman and Hall/CRC, 2015. Chapter 3.

[22] M. Meneghini, G. Meneghesso, and E. Zanoni. *Power GaN Devices; Materials, Applications and Reliability*. Power Electronics and Power Systems. Springer International Publishing, 2017. Chapter 1 and 2.

[23] S. Rajan and D. Jena. Gallium nitride electronics. *Semiconductor Science and Technology*, 28(7):070301, 2013.

[24] F. G. Rammerstorfer. *Lecture Notes - Leichtbau*. ILSB, TU Vienna, 2017.

[25] I. Ratschinski, H. S. Leipner, F. Heyroth, W. Fränzel, G. Leibiger, and F. Habel. The effect of the indenter orientation on the formation of dislocations and cracks in (0001) GaN bulk crystals. *Materials Science Forum*, 725:67–70, 07 2012.

[26] I. Ratschinski, H. S. Leipner, F. Heyroth, W. Fränzel, O. Moutanabbir, R. Hammer, and M. Jurisch. Indentation-induced dislocations and cracks in (0001) freestanding and epitaxial GaN. *Journal of Physics: Conference Series*, 281(1):012007, 2011.

[27] I. Ratschinski, H. S. Leipner, F. Heyroth, W. Mook, J. Michler, W. Fränzel, G. Leibiger, and F. Habel. Cracks and dislocations at vickers, berkovich and cube corner indentations in (0001) GaN single crystals. *Physica Status Solidi C*, 10(1):76–79, 2013.

[28] C. Reichel. Fracture mechanical simulation of indentation testing in gallium nitride. Master's thesis, ILSB, TU Vienna, 2018.

[29] M. Reisinger, J. Zalesak, R. Daniel, M. Tomberger, J. Weiss, A. Darbal, M. Petrenec, J. Zechner, I. Daumiller, W. Ecker, B. Sartory, and J. Keckes. Cross-sectional stress distribution in AlxGa1-xN heterostructure on Si(111) substrate characterized by ion beam layer removal method and precession electron diffraction. *Materials and Design*, 106:476 – 481, 2016.

[30] R. B. Schwarz, K. Khachaturyan, and E. R. Weber. Elastic moduli of gallium nitride. *Applied Physics Letters*, 70(9):1122–1124, 1997.

[31] Y. Tang, A. Yonezu, N. Ogasawara, N. Chiba, and X. Chen. On radial crack and half-penny crack induced by vickers indentation. *Proceedings of the Royal Society of London A: Mathematical, Physical and Engineering Sciences*, 464(2099):2967–2984, 2008.

[32] Tecdia Inc. Diamond indenters. http://us.tecdia.com/products-services/diamond-products-overview/diamond-products-diamond-indenters/. Accessed: 14.05.2018.

[33] A. Turon, C. G. Dávila, P. P. Camanho, and J. Costa. An engineering solution for mesh size effects in the simulation of delamination using cohesive zone models. *Engineering Fracture Mechanics*, 74(10):1665 – 1682, 2007.

[34] C. Yutian, C. Duanjun, W. Hui, W. Jiejun, L. Xiangshun, Z. Guoyi, and Y. Tongjun. Anisotropic fracture toughness of bulk GaN. *Physica Status Solidi B*, page 1700515, 2017.